

Effect of various electron and hole transport layers on the performance of CsPbI₃-based perovskite solar cells: A numerical investigation in DFT, SCAPS-1D, and wxAMPS frameworks

M. Khalid Hossain^{1,2*}, Mirza Humaun Kabir Rubel³, G.F. Ishraque Toki⁴, Intekhab Alam⁵,
Md. Ferdous Rahman⁶, H. Bencherif⁷

¹*Institute of Electronics, Atomic Energy Research Establishment, Bangladesh Atomic Energy Commission, Dhaka 1349, Bangladesh*

²*Department of Advanced Energy Engineering Science, Interdisciplinary Graduate School of Engineering Science, Kyushu University, Fukuoka 816-8580, Japan*

³*Department of Materials Science and Engineering, University of Rajshahi, Rajshahi 6205, Bangladesh*

⁴*College of Materials Science and Engineering, Donghua University, Shanghai 201620, China*

⁵*Department of Mechanical and Manufacturing Engineering, University of Calgary, Calgary, AB T2N 1N4, Canada*

⁶*Department of Electrical and Electronic Engineering, Begum Rokeya University, Rangpur 5400, Bangladesh*

⁷*HNS-RE2SD, Higher National School of Renewable Energies, Environment and Sustainable Development, Batna 05078, Algeria*

Correspondence: * khalid.baec@gmail.com; khalid@kyudai.jp; ORCID: 0000-0003-4595-6367

Abstract

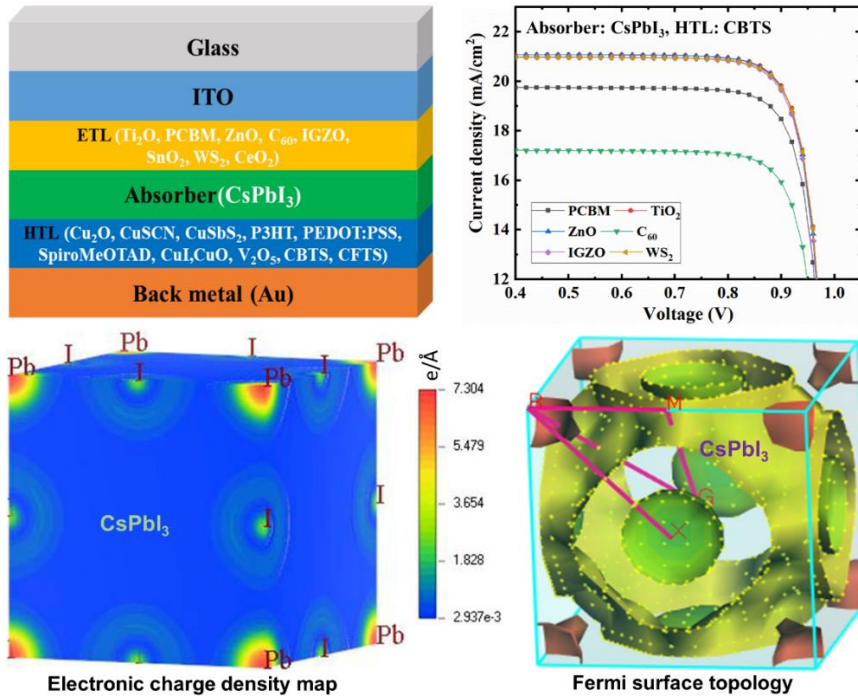
CsPbI₃ has recently received tremendous attention as a possible absorber of perovskite solar cells (PSCs). However, CsPbI₃-based PSCs have yet to achieve the high performance of the hybrid PSCs. In this work, we performed a density functional theory (DFT) study using the Cambridge Serial Total Energy Package (CASTEP) code for the cubic CsPbI₃ absorber to compare and evaluate its structural, electronic, and optical properties. The calculated electronic band gap (E_g) using the GGA-PBE approach of CASTEP was 1.483 eV for this CsPbI₃ absorber. Moreover, the computed density of states (DOS) exhibited the dominant contribution from the Pb-5*d* orbital, and most charge also accumulated for the Pb atom as seen from the electronic charge density map. Fermi surface calculation showed multiband character, and optical properties were computed to investigate the optical response of CsPbI₃. Furthermore, we used IGZO, SnO₂, WS₂, CeO₂, PCBM, TiO₂, ZnO, and C₆₀ as the electron transport layers (ETLs), and Cu₂O, CuSCN, CuSbS₂, Spiro-MeOTAD, V₂O₅, CBTS, CFTS, P3HT, PEDOT: PSS, NiO, CuO, and CuI as the hole transport layers (HTLs) to identify the best HTL/CsPbI₃/ETL combinations using the SCAPS-1D solar cell simulation software. Among 96 device structures, the best-optimized device structure, ITO/TiO₂/CsPbI₃/CBTS/Au was identified, which exhibited an efficiency of 17.9%. The effect of absorber and ETL thickness, series resistance, shunt resistance, and operating temperature was also evaluated for the six best devices along with their corresponding generation rate, recombination rate, capacitance-voltage, current density-voltage, and quantum efficiency characteristics. The obtained results from SCAPS-1D were also compared with wxAMPS simulation software.

Keywords: CsPbI₃ absorber; perovskite solar cell; DFT simulation; SCAPS-1D simulation, wxAMPS simulation; electron transport layer; hole transport layer.

Contents

Effect of various electron and hole transport layers on the performance of CsPbI ₃ -based perovskite solar cells: A numerical investigation in DFT, SCAPS-1D, and wxAMPS frameworks		1
Abstract		1
Graphical Abstract		3
List of abbreviations		3
1	Introduction	4
2	Computational study and numerical simulations.....	5
2.1	First principal calculations of CsPbI ₃ absorber using DFT	5
2.2	SCAPS-1D numerical simulation.....	5
2.3	wxAMPS numerical simulation	6
2.4	CsPbI ₃ -based PSC structure	7
3	Result and discussion	10
3.1	Analysis of DFT results	10
3.1.1	Structural properties of CsPbI ₃ compound	10
3.1.2	Band structure and DOS of CsPbI ₃ solar compound	10
3.1.3	Electron charge density of CsPbI ₃ compound.....	10
3.1.4	Fermi surface of CsPbI ₃ compound	10
3.1.5	Optical properties of CsPbI ₃ compound	11
3.2	Analysis of SCAPS-1D results.....	14
3.2.1	Band diagram and energy level alignment.....	14
3.2.2	Effect of ETL variation.....	15
3.2.3	Effect of HTL variation	16
3.2.4	Effect of absorber and ETL thickness on the device performance.....	17
3.2.5	Effect of series resistance	21
3.2.6	Effect of shunt resistance.....	21
3.2.7	Effect of temperature	22
3.2.8	Capacitance and Mott-Schottky analysis.....	22
3.2.9	Generation and recombination rate analysis	23
3.2.10	J-V and QE characteristics.....	24
3.3	Comparison with wxAMPS results and previous work.....	24
3.3.1	Comparison between SCAPS-1D and wxAMPS results	24
3.3.2	Comparison of SCAPS-1D results with previous work.....	25
4	Conclusion.....	25
Supporting Information		26
Data availability.....		26
Declaration of interests.....		26
Funding Sources		26
Acknowledgments		26
References		26
SUPPORTING INFORMATION.....		33

Graphical Abstract



List of abbreviations

μ_h	Hole mobility	N_t	Defect density
μ_n	Electron mobility	N_V	VB effective density of states
CASTEP	Cambridge serial total energy package	PBE	Perdew-burke-ernzerhif
CBTS	Copper barium thiostannate	PCE	Power conversion efficiency
DFT	Density functional theory	PDOS	Partial density of states
DOS	Density of states	PSC	Perovskite solar cell
EC	Conduction band energy	PV	Photovoltaic
E_g	Band gap	$R(\omega)$	Reflectivity
ETL	Electron transport layer	R_s	Series resistance
EV	Valence band energy	R_{SH}	Shunt resistance
FF	Fill factor	SCAPS-1D	One dimensional solar cell capacitance simulator
GGA	Generalized gradient approximation	TCO	Transparent conductive oxide
HTL	Hole transport layer	TDOS	Total density of states
ITO	Indium doped tin oxide	V_{oc}	Open voltage current
J_e	Electron flux	wxAMPS	Widget provided analysis of microelectronic and photonic structures
J_h	Hole flux	X	Electron affinity
J_{SC}	Short circuit current density	XC	Exchange-correlation functional
$J-V$	Current density-voltage	α	Absorption coefficient
k	Extinction coefficient	$\alpha(\omega)$	Optical absorption
L	Loss function	$\delta(\omega)$	Conductivity
$L(\omega)$	Electron energy loss function	$\varepsilon(\omega)$	Dielectric function
n	Refractive index	ε_1	Real
$n(\omega)$	Refractive index	ε_2	Imaginary
N_A	Shallow uniform acceptor density	ε_r	Dielectric permittivity
N_C	CB effective density of states	λ	Light wavelength
N_D	Shallow uniform donor density	σ	Electrical conductivity
ω_p	Plasma frequency	V_{bi}	Built-in potential
MS	Mott-Schottky	ΔE_f	Formation energy
C-V	Capacitance-voltage	E_F	Fermi level
QE	Quantum efficiency		

1 Introduction

The 21st century is experiencing a massive demand for power, with a substantial amount of need being met by fossil fuels, which pollute the environment and cause the greenhouse effect¹⁻³. A lot of research is being carried out to study the alternate, ecologically suitable energy-generating options, with the solar cell being the most popular and cost-effective option⁴⁻¹⁰. To address future industrial needs, current photovoltaic (PV) investigations are focusing on developing highly efficient devices at cheap manufacturing costs. Even though various studies focus on exceeding the current greatest practicable performance, the PV characteristics are still far below the maximum value^{5,11-14}. Energy shortages and pollutions are the major barriers to the creation of a sustainable society⁴. Therefore, the PV solar cell can be employed as a viable photoelectric conversion system, making this the most potential solution to the problems.

Hybrid halide PSCs, the third generation of PV cells, have received a lot of attention because of their straightforward production technique and cheaper cost¹. The composition of halide perovskite absorber material is denoted as ABX₃, where A is a monovalent cation, B is a divalent metal, and X is a halide anion⁹. Limited exciton binding energy², prolonged carrier lifetime, and high diffusion length¹ along with an excellent absorption coefficient¹⁰ are the important characteristics of these hybrid perovskites. Because of these outstanding PV characteristics, the power conversion efficiency (PCE) of these PSCs has enhanced from 3.8% to 25.5%^{15,16} from the year 2009 to 2020. But because of their poor stability, they are intrinsically unsuited for long-term application in the outdoors^{3,17,18}.

Due to the similar photoelectric characteristics and improved thermal stability compared to the hybrid perovskites, inorganic CsPbI₃-based PSCs have recently gained a lot of attention¹⁹⁻²¹. With a bandgap of around 1.7 eV and exceptional thermal stability, CsPbI₃ is regarded as an excellent material for creating inorganic PSCs²¹. Initially, CsPbI₃-based PSCs had poor PCE compared to the hybrid PSCs. Since then, CsPbI₃-based PSCs have obtained a PCE reaching up to 19.03%²². The optoelectronic characteristics of CsPbI₃ are hindered by the quick transformation of the black perovskite to the yellow orthorhombic non-perovskites at ambient temperature and humidity²³. In a recent simulation conducted with one dimensional solar cell capacitance simulator (SCAPS-1D) software, CsPbI₃-based PSC attained a PCE of 15.6%²⁴, where ZnO and CuSbS₂ were employed as the ETL and HTL, respectively. As shown by the large disparity between the practical and theoretical results, further studies are required to find a better-matched ETL and HTL for CsPbI₃-based PSC.

For the reliability and performance of the PSCs, both ETL and HTL have crucial roles^{24,25}. Inorganic and organic materials such as Al₂O₃, PCBM, C₆₀, ZrO₂, TiO₂, SnO₂, WO_x, ZnO, I₂O₃, BaTiO₃, and PbTiO₃ nanoparticles have been used as the ETL in the PSCs over the years²⁴⁻²⁹. Due to the wide band gap, better energy level, and environmental stability, TiO₂ is one of the highly utilized ETLs³⁰. Also, the suitable band gap, good stability, and desirable band bending make TiO₂ as one of the best ETLs to be used with the CsPbI₃ perovskite absorber material. The TiO₂ nanostructures, including nanotubes, nanosheets, nanoparticles, nanorods, and nanowires, have been employed as the ETL in high-performing PSCs^{25,26}. The TiO₂ ETL has been widely used to remove and transfer the photo-generated electrons and protect the transparent conductive oxide (TCO) from interacting with the HTL³¹. As a result, there is an imbalance between the electron flux (J_e) and hole flux (J_h) owing to the lower charge mobility of TiO₂ as compared to the charge mobilities of the most commonly employed HTLs³². Therefore, one of the primary issues with the TiO₂-based planar PSCs is the hysteresis of the current density-voltage ($J-V$) relationship³³.

High-performance PV devices are difficult to fabricate because of the poor efficiency of carrier extraction³⁴. The performance, durability, and production cost of the solar cells are influenced by the HTL and its neighboring surfaces^{25,35}. Small molecule HTLs enable the solar cells to perform better, but they don't have enough thermal and photo-stability. Contrarily, polymeric HTLs are attractive because they are stable at high temperatures, repel water, and are compatible with other materials^{25,26}. But these HTLs may have disadvantages such as poor optoelectronic properties, which can cause less efficiency. The HTLs made of inorganic materials are more chemically stable and cheaper than those fabricated from organic materials³⁶. The rising need for low-cost solar cell production encourages the use of earth-abundant, air-stable thin-film materials such as copper barium thiostannate (CBTS) as the HTL, instead of the more commonly used Cu₂O, CuSCN, CuSbS₂, NiO, P3HT, PEDOT: PSS, Spiro-MeOTAD, CuI, CuO, and V₂O₅ HTLs, due to its tunable bandgap and good light-absorbing

capabilities. Among the cation elements, the noncentrosymmetric crystal structure and substantial atomic size variations of CBTS ensure favorable characteristics to improve the PCE of the PV cells^{35,37,38}. Previous studies have also mentioned that the CBTS HTL has good properties because of its appropriate absorption coefficient and electron affinity^{35,38}.

In this work, initially, the symmetric, electronic, as well as optical properties of the CsPbI₃ absorber have been evaluated by the first-principle computations in the framework of DFT by employing CASTEP software. Then we attempted to determine the optimized combinations of ETL and HTL with the CsPbI₃ absorber to enhance the device's performance by performing SCAPS-1D numerical investigations as it is time-consuming and expensive to investigate all possible combinations experimentally. However, very few theoretical investigations have been conducted for the CsPbI₃ absorber as compared to the other absorbers, and most of them are limited to enhancing the device performance by modifying various parameters only. Therefore, we have conducted a study on several HTLs (Cu₂O, CuSCN, CuSbS₂, NiO, P3HT, PEDOT: PSS, Spiro-MeOTAD, CuI, CuO, V₂O₅, CBTS, and CFTS) and ETLs (PCBM, TiO₂, ZnO, C₆₀, IGZO, SnO₂, WS₂, and CeO₂) (**Table 1** and **2**) to find the best combination. After that, for the best six devices, we checked the effect of absorber and ETL thickness, series resistance, shunt resistance, and working temperature on the device performance along with their band diagram, capacitance-voltage (*C-V*), generation rate, recombination rate, *J-V*, and quantum efficiency (*QE*) characteristics. Finally, the performance parameters of these structures have been validated with the widget provided analysis of microelectronic and photonic structures (wxAMPS) simulation software.

2 Computational study and numerical simulations

2.1 First principal calculations of CsPbI₃ absorber using DFT

Herein, the computational studies using DFT in the framework of the CASTEP code³⁹ were accomplished to compare and correlate the properties. In this approach, the generalized gradient approximation (GGA) to the exchange-correlation potential with the parameter Perdew-Burke-Ernzerhif (PBE)^{39,40} was applied, where ultrasoft pseudopotential rituality of the Vanderbilt type⁴¹ was set for all elements interactions between valence electrons and ion ores. As the selection of exchange-correlation functionals (XCs) is an important parameter for DFT calculations, thus we optimized the structure with Pm3m symmetry of cubic phase. Broyden-Fletcher-Goldfarb-Shannon (BFGS) algorithm⁴² was exploited with different XCs to find the minimum energy state of the complete stable structure. The formation energy (ΔE_f , eV/atom) in the optimized structure and the calculated lattice constants are mainly compared with the reported experimental data. The best-produced data by XC was applied to compute all the characteristics of CsPbI₃ material. Cutoff energy of 520 eV was set in the wave function for the computational study of the CsPbI₃ solar absorber. Monkhorst-Pack grid⁴³ of $12 \times 12 \times 12$ (*k*-point) was applied for modeling the irreducible Brillouin zone. On the other hand, a greater scale of *k*-point mesh $17 \times 17 \times 17$ was employed to observe the electronic charge density map and Fermi surface topology, evidently. In these calculations, 1×10^{-6} eV/atom (full energy) was used for the convergence tolerances of geometry optimization, 0.03 eV/Å was the highest potency on atoms, 0.001 Å was the maximal displacement of atoms, and 0.05 GPa was the maximum stress.

2.2 SCAPS-1D numerical simulation

The simulation model makes it easier to comprehend the fundamentals of solar cells and identifies the major factors that influence how well they function. The SCAPS-1D software^{44,45} numerically solves the one-dimensional equations that influence the conduction of the semiconductor materials' charge carriers when they are in a stable state. Poisson's equation, which describes the connection between the electric field (*E*) of a p-n junction and the space charge density (ρ), is presented in **Eq. (1)**:

$$\frac{d}{dx} \left(-\varepsilon(x) \frac{d\psi}{dx} \right) = q[p(x) - n(x) + N_d^+(x) - N_a^-(x)] \quad (1)$$

Here, ε denotes the permittivity, q denotes the electron charge, ψ denotes the electrostatic potential, n is the total electron density, p represents the total hole density, N_d^+ represents the ionized donor-like doping concentration, and N_a^- denotes the ionized acceptor-like doping concentration. **Eqs. (2)** and **(3)**, regarded as the electron and holes continuity equations, are given below:

$$\frac{\partial j_n}{\partial x} = q(R_n - G + \frac{\partial n}{\partial t}) \quad (2)$$

$$\frac{\partial j_p}{\partial x} = -q(R_p - G + \frac{\partial p}{\partial t}) \quad (3)$$

Here, j_n symbolizes the electron density, j_p stands for the hole's current density, R_n denotes the net recombination rates for the electrons per unit volume, R_p is the net recombination rate for the holes per unit volume, and G is the generation rate per unit volume.

In this work, the new E_g -sqrt model, which is the updated version of the previous SCAPS model (the conventional sqrt ($h\nu - E_g$) law model), was used to calculate the absorption constant for each layer. This model can be found from the "Tauc laws". The E_g -sqrt model is described in **Eq. (4)**:

$$\alpha(h\nu) = (\alpha_0 + \beta_0 \frac{E_g}{h\nu}) \sqrt{\frac{h\nu}{E_g} - 1} \quad (4)$$

Here, α denotes the optical absorption constant, $h\nu$ implies the photon energy, and E_g symbolizes the bandgap. The model constants, α_0 and β_0 , have the dimension of the absorption constant (e.g., cm^{-1}) and are related to the conventional model constants A and B by the following **Eqs. (5)** and **(6)**:

$$\alpha_0 = A \sqrt{E_g} \quad (5)$$

$$\beta_0 = \frac{B}{\sqrt{E_g}} \quad (6)$$

2.3 wxAMPS numerical simulation

In wxAMPS numerical simulation, Poisson's equation in 1-D space is used, which is given in **Eq. (7)**⁴⁶:

$$\frac{d}{dx} \left(-\varepsilon(x) \frac{d\psi'}{dx} \right) = q \cdot [p(x) - n(x) + N_D^+(x) - N_A^-(x) + pt(x) - nt(x)] \quad (7)$$

Where, the electrostatic potential is denoted by ψ' , the concentrations of the ionized donor-like and acceptor-like dopants are denoted by N_D^+ and N_A^- , respectively, the free electron is indicated by n , the free hole is symbolized by p , the trapped electron is represented by nt , and the trapped hole is denoted by pt . All of them are the variables of the position coordinate, x . The free electron carriers in the delocalized states of the conduction bands are represented by the following formula (**Eq. (8)**)⁴⁷:

$$\frac{1}{q} \left(\frac{dJ_n}{dx} \right) = -G_{op}(x) + Rx \quad (8)$$

The continuity equation in the case of the free holes in the delocalized states of the valence band has been illustrated in **Eq. (9)**⁴⁷:

$$\frac{1}{q} \left(\frac{dJ_p}{dx} \right) = G_{op}(x) - Rx \quad (9)$$

Where, J_n and J_p are denoted by the electron and hole current densities, respectively. The parameter $R(x)$ is used for the net recombination rate that results from the band-to-band recombination and Shockley-Read-Hall (SRH) recombination traffic via the gap states. The total direct recombination rate is given in **Eq. (10)**⁴⁸:

$$R_D(x) = \beta(np - ni^2) \quad (10)$$

Where, n and p are the existing band carrier concentrations when the devices are exposed to a voltage bias, light bias, or even both, and β represents the proportionality constant based on the material's band structure under investigation. The term $G_{op}(x)$ is used for the optical generation rate as a function of x owing to the externally applied light, which is included in the continuity equation.

2.4 CsPbI₃-based PSC structure

The simulations were conducted for CsPbI₃-based PSC in this study that had an n-i-p planar heterojunction. The ETL, perovskite layer, and HTL were positioned in the n-region, i-region, and p-region, respectively. Exciton, a confined state consisting of an electron and a hole, is formed in the perovskite layer of the device when the cell is exposed to light. According to the length of their diffusion, they are capable to enter the n (p) area. The exciton splits apart at the interface between the n-layer and i-layer, sending the electrons and residual holes in the direction of the n-layer and p-layer, respectively. In a similar manner, the exciton splits apart at the interface between the i-layer and p-layer, causing the holes to go to the p-layer, while the residual electrons travel to the n-layer. The electrical field that exists between these layers helps to facilitate the dissociation of excitons, as well as the movement of electrons and holes.

Throughout the simulation, as the TCO, absorber, and back contact, the indium-doped tin oxide (ITO), CsPbI₃ perovskite (**Table 1**), and Au were employed, respectively. Furthermore, eight ETLs and twelve HTLs (**Table 1** and **Table 2**) were investigated for the PSC to explore the best combination. For each ETL in **Table 1**, we studied twelve different HTLs (**Table 2**) to get the best combination structures from 96 different combinations (**Figure 1(a)**). Additionally, the inclusion of interface defect layers is also supported by the SCAPS-1D software package. **Table 3** provides a summary of the defect density that was applied at each of the interfaces. Apart from evaluating the effect of working temperature on the device's efficiency, the simulations were conducted at a frequency and working temperature of 1 MHz and 300 K, respectively, under the AM1.5G 1 solar spectrum along with an incident power density of 1000 mW/cm².

Table 1. Input parameters of the ITO, ETLs, and absorber layer.

Parameters	ITO	TiO ₂	PCBM	ZnO	C ₆₀	IGZO	SnO ₂	WS ₂	CeO ₂	CsPbI ₃
Thickness (nm)	500	30	50	50	50	30	100	100	100	800*
Band gap, E _g (eV)	3.5	3.2	2	3.3	1.7	3.05	3.6	1.8	3.5	1.694
Electron affinity, χ (eV)	4	4	3.9	4	3.9	4.16	4	3.95	4.6	3.95
Dielectric permittivity (relative), ϵ_r	9	9	3.9	9	4.2	10	9	13.6	9	6
CB effective density of states, N _C (1/cm ³)	2.2×10^{18}	2×10^{18}	2.5×10^{21}	3.7×10^{18}	8.0×10^{19}	5×10^{18}	2.2×10^{18}	1×10^{18}	1×10^{20}	1.1×10^{20}
VB effective density of states, N _V (1/cm ³)	1.8×10^{19}	1.8×10^{19}	2.5×10^{21}	1.8×10^{19}	8.0×10^{19}	5×10^{18}	1.8×10^{19}	2.4×10^{19}	2×10^{21}	8.2×10^{20}
Electron mobility, μ_n (cm ² /Vs)	20	20	0.2	100	8.0×10^{-2}	15	100	100	100	25
Hole mobility, μ_h (cm ² /Vs)	10	10	0.2	25	3.5×10^{-3}	0.1	25	100	25	25
Shallow uniform acceptor density, N _A (1/cm ³)	–	–	–	–	–	–	–	–	–	1×10^{15} *
Shallow uniform donor density, N _D (1/cm ³)	1×10^{21}	9×10^{16}	2.93×10^{17}	1×10^{18}	1×10^{17}	1×10^{17}	1×10^{17}	1×10^{18}	10^{21}	0*
Defect density, N _t (1/cm ³)	1×10^{15} *	1×10^{15} *	1×10^{15} *	1×10^{15} *	1×10^{15} *	1×10^{15} *	1×10^{15} *	1×10^{15} *	1×10^{15} *	1×10^{15} *
References	26,49,50	25,26	27–29,49,51	25,52	27	53,54	25,51	26,55	56	24

*In this study, these values remain constant during initial optimization to get the best combination of HTL, ETL, and back metal contact

Table 2. Input parameters of the HTLs.

HTL	Cu ₂ O	CuSCN	CuSbS ₂	P3HT	PEDOT: PSS	Spiro- MeOTAD	NiO	CuI	CuO	V ₂ O ₅	CFTS	CBTS
Thickness (nm)	50	50	50	50	50	200	100	100	50	100	100	100
Band gap, E _g (eV)	2.2	3.6	1.58	1.7	1.6	3	3.8	3.1	1.51	2.20	1.3	1.9
Electron affinity, χ (eV)	3.4	1.7	4.2	3.5	3.4	2.2	1.46	2.1	4.07	4.00	3.3	3.6
Dielectric permittivity (relative), ϵ_r	7.5	10	14.6	3	3	3	10.7	6.5	18.1	10.00	9	5.4
CB effective density of states, N _C (1/cm ³)	2×10^{19}	2.2×10^{19}	2×10^{18}	2×10^{21}	2.2×10^{18}	2.2×10^{18}	2.8×10^{19}	2.8×10^{19}	2.2×10^{19}	9.2×10^{17}	2.2×10^{18}	2.2×10^{18}
VB effective density of states, N _V (1/cm ³)	1×10^{19}	1.8×10^{18}	1×10^1	2×10^{21}	1.8×10^{19}	1.8×10^{19}	1×10^{19}	1×10^{19}	5.5×10^{20}	5.0×10^{18}	1.8×10^{19}	1.8×10^{19}
Electron mobility, μ_n (cm ² /Vs)	200	100	49	1.8×10^{-3}	4.5×10^{-2}	2.1×10^{-3}	12	100	100	3.2×10^2	21.98	30
Hole mobility, μ_h (cm ² /Vs)	8600	25	49	1.86×10^{-2}	4.5×10^{-2}	2.16×10^{-3}	2.8	43.9	0.1	4.0×10^1	21.98	10
Shallow uniform acceptor density, N _A (1/cm ³)	1×10^{18}	1×10^{18}	1×10^{18}	1×10^{18}	1×10^{18}	1×10^{18}	1×10^{18}	1×10^{18}	1×10^{18}	1×10^{18}	1×10^{18}	1×10^{18}
Shallow uniform donor density, N _D (1/cm ³)	-	-	-	-	-	-	-	-	-	-	-	-
Defect density, N _t (1/cm ³)	$1 \times 10^{15*}$	$1 \times 10^{15*}$	$1 \times 10^{15*}$	$1 \times 10^{15*}$	$1 \times 10^{15*}$	$1 \times 10^{15*}$	$1 \times 10^{15*}$	$1 \times 10^{15*}$	$1 \times 10^{15*}$	$1 \times 10^{15*}$	$1 \times 10^{15*}$	$1 \times 10^{15*}$
References	25,57	25	25	25	58,59	25,26,60	61	62	63	64	35	35

*In this study

Table 3. Input parameters of the interface defect layers ²⁵.

Interface	Defect type	Capture cross-cpection: Electrons/holes (cm ²)	Energetic distribution	Reference for defect energy level	Total density (cm ⁻²) (integrated over all energies)
ETL/CsPbI ₃	Neutral	1.0×10^{-17} 1.0×10^{-18}	Single	Above the VB maximum	1.0×10^{10}
CsPbI ₃ /HTL	Neutral	1.0×10^{-18} 1.0×10^{-19}	Single	Above the VB maximum	1.0×10^{10}

3 Result and discussion

3.1 Analysis of DFT results

3.1.1 Structural properties of CsPbI₃ compound

The crystal structure of the single-cubic-perovskite CsPbI₃ solar absorber with Pm3m space group (No. 221) is shown in **Figure 1(b)**. In the structure, there is a single formula unit with 5 atoms, where Cs is at the body center position, Pb occupies the corner position, and I is at the face center of the cube. The calculated lattice parameter of the best-optimized structure of CsPbI₃ was 6.407 Å, which excellently matches the experimental data (6.414 Å). Very consistent lattice parameters and negative formation energy (-6.905 eV/atom) indicate the cell stability of the solar cell absorber material as well.

3.1.2 Band structure and DOS of CsPbI₃ solar compound

The electronic band diagram and corresponding density of states (DOS) of CsPbI₃ cubic perovskite towards the better symmetry directions (X-R-M-Γ-R) of the Brillouin zone are presented in **Figures 1(c)** and **1(d)**, respectively. The Fermi level (E_F) in these figures is shown by a horizontal dotted line. It is well recognized that photon-absorbing materials (solar cells) always exhibit band gap (E_g) energy that belongs to the class of semiconducting substances. From **Figure 1(c)**, it is obvious that there is a direct band gap, $E_g \sim 1.48$ eV for the CsPbI₃ while applying the GGA-PBE method, which is somewhat lower than the previous report (1.694 eV)²⁴. This discrepancy in band gap energy might be originated because of the utilization of GGA-PBE potential (average potential) that generally debates the band gap of semiconductors^{65,66}. **Figure 1(d)** depicts the total density of states (TDOS) and partial density of states (PDOS) that show the contributions of different orbital electrons, as well as the chemical bonding nature of CsPbI₃. The shown TDOS curve indicates that the compound has n-type carriers with a small value of TDOS (1.98 states/eV) at E_F owing to its semiconducting nature. The occurred individual band PDOS from Pb-5*d* orbital electrons contributes mostly in contrast to any other orbital electrons at E_F , whereas the Cs-6*s* orbital has a moderate contribution, and I-5*p* has a trivial effect in the vicinity of E_F for the generation of carriers. Therefore, amid the PDOS of CsPbI₃, the Pb atom orbital electrons play key roles in the absorption of photon energy and hence the generation of photocurrent.

3.1.3 Electron charge density of CsPbI₃ compound

Figure 1(e) displays the charge density map toward the (100) crystallographic plan, where the scale bar on the right side implies the intensity of electron density according to colors. It is observed that the charges gather dominantly around the Pb atom, and the charge ordering around Pb is identical also. The Pb-I bond is punchy owing to the hybridization between Pb-5*d* and I-5*p* orbitals, which is also seen from the DOS curve. Nonetheless, the Cs atom in the charge density figure is not visualized separately because of the charge overlapping of Cs with the I-atom. Moreover, the charge distribution map revealed that the Cs and I ions create an ionic bond, while the covalent bond was found for the Pb and I ions. This covalent nature of Pb and I ion is used to create a weaker bond, whereas the ionic bond increases the bonding nature in the structural unit. In this structure, the covalent bond occurred due to the hybridization of Pb-5*d* and Cs-6*s* states^{67,68}. It is found that the charge distribution is almost spheric around the entire atoms, which is a signature of ionic bonding that can be compared with reported perovskites⁶⁹⁻⁷¹ as well. Furthermore, the electronic charge density maps along different crystal planes originated identical results, which is an indication of its isotropic behavior.

3.1.4 Fermi surface of CsPbI₃ compound

The computed Fermi surface topology at different paths of the Brillouin zone of the CsPbI₃ solar absorber is depicted in **Figure 1(f)**. It is visualized that at the R(0.5,0.5,0.5) point of each corner, a separated small hole-like rectangular curve shape sheet is connected with a circular disc/plate-like electron sheet at X(0.5,0.0,0.0) point of body center. There are six electron-like sheets that are found on six faces of the cube. Moreover, six hole-like spheroid giant hollow sheets are also present at the body centers by covering the path R-M-Γ-R, where the R-point is directly linked with the center Γ(0.0,0.0,0.0) point in the topology of the Fermi surface. Therefore, both electron-like and hole-like Fermi surfaces exist, which indicates the multi-band feature of the titled material.

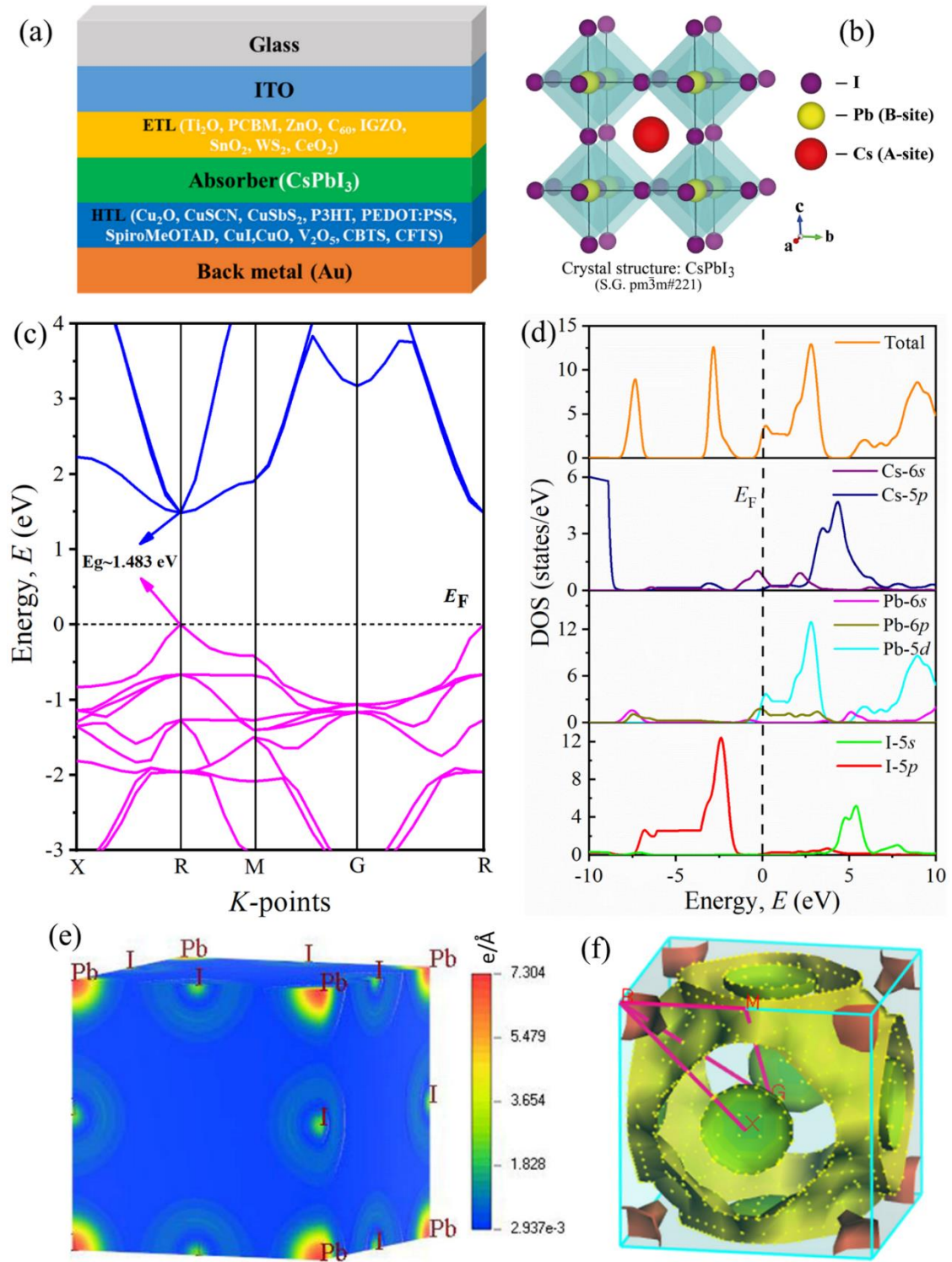


Figure 1. (a) Design configuration of the CsPbI₃-based PSC, (b) the crystal structure of CsPbI₃ cubic-single-perovskite semiconductor, (c) computed band structure along noted symmetry direction of Brillouin zone using GGA-PBE approach, (d) total and partial density of states of CsPbI₃ semiconductor, (e) electronic charge density map along (100) plane, and (f) Fermi surface topology of CsPbI₃ semiconductor perovskite.

3.1.5 Optical properties of CsPbI₃ compound

The optical functions are very important to study the electronic structure and potential optical applications in the arena of optoelectronics as well as nano-electronic devices. Therefore, in this study, we calculated frequency-dependent six optical parameters such as dielectric function ($\epsilon(\omega)$), electron energy loss function ($L(\omega)$), refractive index ($n(\omega)$), optical absorption ($\alpha(\omega)$), reflectivity ($R(\omega)$), and conductivity ($\delta(\omega)$). The calculated

optical characteristics of CsPbI₃ solar absorber material and its architectures were investigated from the energy range of 0 to 40 eV, where the real (ϵ_1) and imaginary (ϵ_2) parts are shown by solid and broken/dotted lines, respectively, in **Figures 2(a)-(c)**.

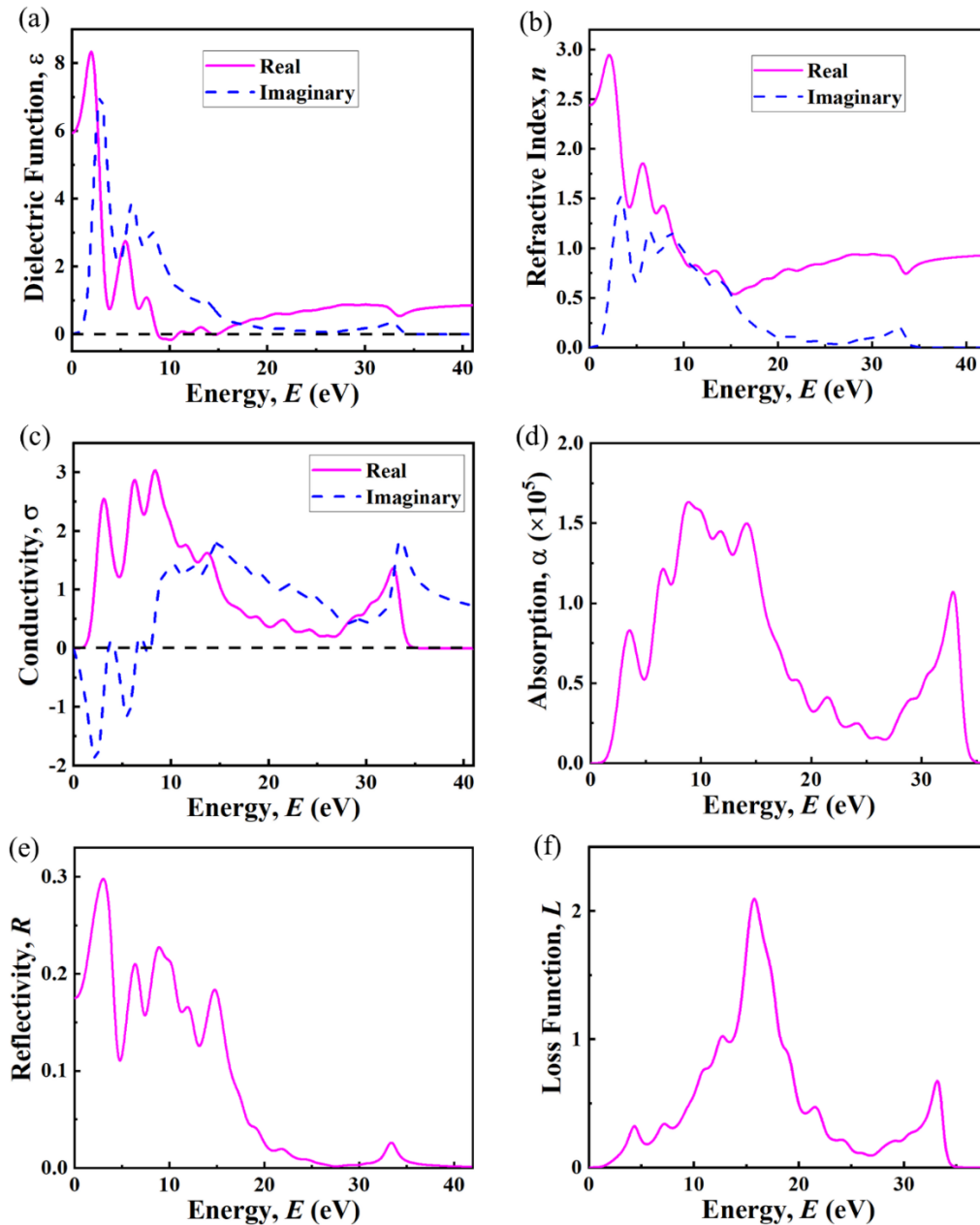


Figure 2. Frequency-dependent optical properties of CsPbI₃: (a) dielectric function (ϵ), (b) refractive index (n). Frequency-dependent optical properties of CsPbI₃: (c) photoconductivity (σ), (d) absorption coefficient (α), (e) reflectivity (R), and (f) loss function (L).

Figure 2(a) represents the real (ϵ_1) and imaginary (ϵ_2) spectra in terms of the photon energy of CsPbI₃, where ϵ_1 of real dielectric function at zero energy is regarded as the electronic portion of static dielectric function that has the exactly 6.0 value at zero frequency. The ϵ_1 gradually increases with the increment of photon energy and reaches the apex value of 8.26 at around 2.64 eV. After that, it sharply drops to a lower dielectric function and again rises at 4.96 eV. Next, another peak is seen at 7.54 eV. However, ϵ_1 reaches down to zero at 8.86 eV and returns to zero again at around 10.56 eV. The observed negative dielectric function in this frequency range is an indication of the Drude-like behavior of the material. In addition, the dielectric function is related to intra and inter band transitions, where intra band transition generally occurs due to the absorption of free or conduction electrons for metal systems. There are three main observed peaks at 2.64 eV, 4.96 eV, and 7.54 eV in the

investigated frequency region. Among these, the highest peak at 2.64 eV in the visible region originated owing to the inter band transitions of electrons, whereas the other two low-intensity peaks are found for the lower intensities of semi-core states of the conduction bands. From 20.12 eV to 32.68 eV, the dielectric function exhibits an almost linear response with an increase in frequency. There was a certain amount of energy loss due to the electrons. In this range of frequency, the energy loss originates due to the electron transitions, and the dielectric function becomes almost zero or negative. Thus, no wave propagated from this region⁷². Notably, the imaginary dielectric function, $\varepsilon_2(\omega)$ attains zero in the ultraviolet spectrum at about 25 eV, which proves the transparent character and optically anisotropic nature of CsPbI₃ as well.

The parameters refractive index (n) and extinction coefficient (k) deal with the absorption loss, as well as the changes in the phase velocity during the propagation of the electromagnetic signal (light) throughout the compounds. The computed frequency-dependent n and k spectra are displayed in **Figure 2(b)**, where $n(0) = 2.45$ is seen for the CsPbI₃ solar absorber⁷². We notice that the refractive index increases with the increment of radiative light (2.08 eV), and the highest value of the refractive index was 2.98. Moreover, at 5.63 eV and 7.87 eV energies, the refractive indexes were 0.87 and 1.43, respectively, meaning that the refractive index varies with the external frequency, which is an indication of the photorefractive properties of CsPbI₃. However, the found value of $n(0)$ of the material is comparable with the K₂Cu₂GeS₄ and GaAs semiconductors⁷³.

Figure 2(c) shows the spectra of photoconductivity, where the changes of electrical conductivity (σ) are very analogous to that of absorption coefficient (α). It is seen from **Figure 2(c)** that the real portion of the σ commences from zero frequency, though CsPbI₃ is a moderate band gap (1.489 eV) semiconductor as seen from the band diagram of **Figure 1(d)**. The aforementioned phenomenon might be originated due to a lack of more accurate potentials and the degenerate semiconducting nature or high electrical conducting behaviour of Pb-6p/5d and Cs-6s orbital electrons at E_F (**Figure 1(d)**). Thus, it is uttered that the studied material behaves like a degenerate semiconductor, which is a convenient feature for high-efficiency solar cell applications. However, in the case of photoconductivity, three prominent peaks appeared in the range of 4.5 eV to 9.8 eV, where the highest magnitude (3.03) peak is observed at 9.79 eV. After reaching the maximal value, the photoconductivity tends to reduce with photon energy.

The optical function, α shows the number of photons absorbed by the substances, as well as provides important data about the conversion efficiency of solar energy⁷⁴. **Figure 2(d)** reveals the α curve of CsPbI₃ that is involved with the optimal solar energy altering efficiency and initiates with approximately 1.48 eV because of the semiconducting character along with the predicted band gap, as well as visualized from the band diagram. Commonly, it is observed that the peaks in the low energy infrared range originate from the intra band transition⁷², whereas the peaks in the exalted-frequency level of absorption and conductivity spectra are seen forasmuch as the inter band transitional nature. It is seen that three main absorption peaks arise in the extent of 7 eV to 14 eV, which originate due to the absorption of photons from the ultraviolet energy region. Among these, the utmost absorption is discovered at 8.64 eV owing to the intra band transition. In contrast, other high-level intensity peaks from 18 eV to 30 eV arise for the inter band electronic transition rates. Importantly, the σ , and hence, the photoconductivity of a semiconductor material raises with absorbed lights⁷⁵ and exhibits a similar trend like the α function.

Figure 2(e) represents the frequency-dependent reflectivity spectrum (R) for CsPbI₃, which is an important optical function for the determination of all optical constants by employing the Kramers-Kronig relations. From **Figure 2(e)**, we see that the R -value started at zero energy is considered as the static part of reflectivity, where the highest reflectivity (0.3) is visualized in the infrared region (3.85 eV) for the intra band transition in the compound. Moreover, the $R(0) = 1.75$ is observed for this solar cell absorber. Furthermore, few peaks with low intensity are found for it in the ultraviolet range owing to the inter band transitions. We also noticed that the reflectivity declines with the increment of the energy band gap^{72,76} in the material.

Figure 2(f) shows the energy loss spectrum (L) of CsPbI₃, which indicates how much energy a fast electron loses during propagating through a compound. The maximal loss function (L) is associated with the plasma resonance, and its consorted frequency is called the plasma frequency, ω_p ⁷⁷. The highest peak value (2.1) for this compound is observed at 15.91 eV, which indicates the plasma frequency of the perovskite. It is seen that the main energy loss occurs in the ultraviolet region due to the higher photon energy than the band gap energy⁷². However,

the relatively low value of ω_p and L might be originated because of the semiconducting behavior and/or the bigger effective mass of the conduction electrons.

3.2 Analysis of SCAPS-1D results

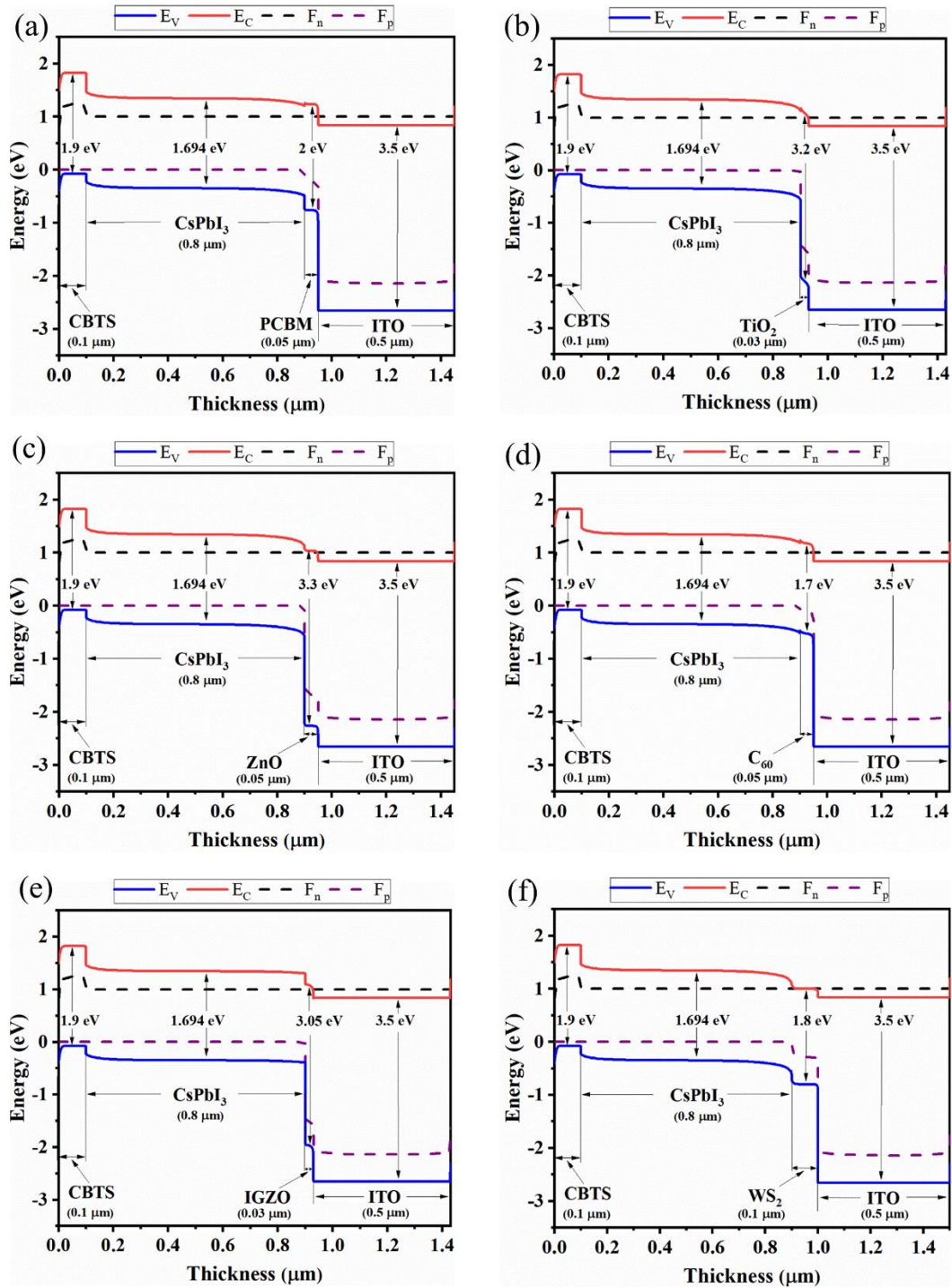


Figure 3. Energy diagram of CsPbI₃-based PSCs with CBTS as the HTL and (a) PCBM, (b) TiO₂, (c) ZnO, (d) C₆₀, (e) IGZO, and (f) WS₂ as the ETL.

3.2.1 Band diagram and energy level alignment

Figure S1 shows the energy level alignment of the studied CsPbI₃ absorber, ITO, ETLs, and HTLs, and **Figure 3** shows the energy diagram of CsPbI₃-based best optimized six (06) PSCs. To extract the electron at the ETL/CsPbI₃ interface, the electron affinity of ETL must be greater than that of CsPbI₃, whereas the ionization energy of CBTS HTL must be less than that of CsPbI₃ to extract the holes at the CsPbI₃/HTL interface. Additionally,

the energy band imbalance at both interfaces has a considerable impact on the performance parameters of the device (**Figure 3**). In **Figure 3**, each device's quasi-Fermi levels, F_n and F_p , cohabited with conduction band energy (E_c) and valence band energy (E_v), respectively. In each ETL, the F_p was superimposed over the E_v , while the F_n and E_c carried on in a manner that was harmonically comparable. The bandgap of CsPbI_3 was 1.694 eV, whereas the bandgaps of PCBM, TiO_2 , ZnO, C_{60} , IGZO, and WS_2 ETLs were 2 eV, 3.2 eV, 3.3 eV, 1.7 eV, 3.05 eV, and 1.8 eV, respectively (**Figure S1**). Due to the similar nature of band alignment, the performance of the TiO_2 and ZnO ETLs was relatively similar. On the other hand, it was discovered that the F_n was able to pass through the E_c , but the F_p and E_v continued to exist at the same level in the CBTS HTL compared to other HTLs (**Figure 3**). This kind of behavior prevents the holes from moving into the ETL and electrons from moving toward the HTL. As a direct consequence of this, the rear contact is able to readily collect holes from the CBTS HTL, while the front contact is able to simply collect electrons from the CsPbI_3 absorber layer. As a result of this idea, the rear contact was made of gold, which had a work function of 5.1 eV, while the TCO was made of indium dioxide, which held a work function of 4.0 eV. On the other hand, PCBM, C_{60} , and IGZO ETLs showed relatively lower performance because of their corresponding bandgaps (**Figure S1**).

3.2.2 Effect of ETL variation

The performance of CsPbI_3 -based PSC was optimized by employing different configurations of 12 HTLs and 8 ETLs while keeping Au as the back contact. However, as SnO_2 and CeO_2 ETLs showed very poor performance, they were disregarded while plotting the performance graphs for different combinations as shown in **Figure 4**.



Figure 4. Performance of CsPbI_3 -based PSC for various HTLs with Au as the back contact and (a) PCBM, (b) TiO_2 , (c) ZnO, (d) C_{60} , (e) IGZO, and (f) WS_2 as the ETL.

During the optimization, the absorber thickness, acceptor density, donor density, and defect density were kept constant at 800 nm, 10^{15} cm^{-3} , 0 cm^{-3} , and 10^{15} cm^{-3} , respectively, for finding out the best configuration of ETL and HTL. In addition, for each HTL, ETL, and ITO, the defect density was 10^{15} cm^{-3} . The best 6 configurations of PSC to achieve the highest PCE by using a variety of ETLs with the best HTL are mentioned in **Table 4**. **Figure 4** and **Table 4** illustrate that the ITO/TiO₂/CsPbI₃/CBTS/Au configuration achieved the highest PCE of 17.90%, with a short circuit current density (J_{SC}) of 21.075 mA/cm², field factor (FF) of 85.21%, and open circuit voltage (V_{OC}) of 0.997 V. From **Figure 4**, we found that ETLs like TiO₂, ZnO, WS₂, and IGZO achieved nearly 18% PCE due to their band alignment in comparison to other ETLs such as C₆₀, PCBM, CeO₂, and SnO₂ (**Figure S1**). When being employed with TiO₂ ETL, the HTLs like Cu₂O, CuSCN, and CBTS achieved significant PCEs of 17.64%, 17.81%, and 17.90%, respectively, whereas ZnO and WS₂ ETLs achieved similar PCEs (>17.5%) while being used with those HTLs. From the energy diagrams (**Figure 3**), it was observed that TiO₂ and ZnO ETLs were positioned closer, and the bandgap of TiO₂ and ZnO was 3.2 eV and 3.3 eV, respectively. Because of that, the configurations with TiO₂ and ZnO as the ETL showed very close PCE of 17.9% and 17.86%, respectively. In a few studies, both of them showed an efficiency of around 25% when used as the ETL⁷⁸. To find better-optimized results, the thickness, donor density, and defect density of these ETLs were optimized in the previous findings enlisted in **Table 1**^{25,26,52}. After considering all the aspects, 6 best-performed ETLs were considered for the onward study (**Table 4**).

Table 4: Performance parameters for the combinations of different ETLs with the best HTL.

Optimized Device	V_{oc} (V)	J_{sc} (mA/cm ²)	FF (%)	PCE (%)
ITO/PCBM/CsPbI ₃ /CBTS/Au	0.994	19.77	85.04	16.71
ITO/TiO ₂ /CsPbI ₃ /CBTS/Au	0.997	21.07	85.21	17.90
ITO/ZnO/CsPbI ₃ /CBTS/Au	0.997	21.07	85.03	17.86
ITO/C ₆₀ /CsPbI ₃ /CBTS/Au	0.990	17.25	84.80	14.47
ITO/IGZO/CsPbI ₃ /CBTS/Au	0.995	20.98	85.13	17.76
ITO/WS ₂ /CsPbI ₃ /CBTS/Au	0.997	20.98	85.22	17.82

3.2.3 Effect of HTL variation

When eight sets of ETLs were optimized with twelve separate HTLs, compared to the other HTLs, the CBTS, CuSCN, CuI, and Cu₂O HTLs showed superior PCEs of around 17% to 18% for all the ETLs except C₆₀, CeO₂, and SnO₂ ETLs. When viewed from the perspective of the band diagram, these HTLs seemed to be most suited for the CsPbI₃ absorber. On the other hand, in contrast to the other HTLs, the V₂O₅ and CFTS HTLs showed lower PCEs of 0.6% and <8%, respectively, when paired with each ETL (**Figures S1 and 4**). As HTL is a p-type layer, it has to be thicker in contrast to the n-type ETL to lower the possibility of recombination. Because this permits the quick transfer of an equal number of charge carriers to the device⁷⁹. As a consequence, the thickness of each ETL was smaller in comparison with the corresponding HTL. When we tested the inorganic HTLs, we found that they performed better than the organic HTLs in most cases with some exceptions. This is because the inorganic HTLs have features such as increased stability, high transparency, and good band alignment. For each case of **Figure 4**, we found that CBTS HTL, an earth-abundant material, showed excellent results for each ETL due to its excellent crystalline structure, light-absorbing ability, and atomic size^{35,37,38}. **Figure S2** illustrates the best-optimized structures of CsPbI₃-based PSC with CBTS as the HTL and PCBM, TiO₂, ZnO, C₆₀, IGZO, and WS₂ as the ETLs.

3.2.4 Effect of absorber and ETL thickness on the device performance

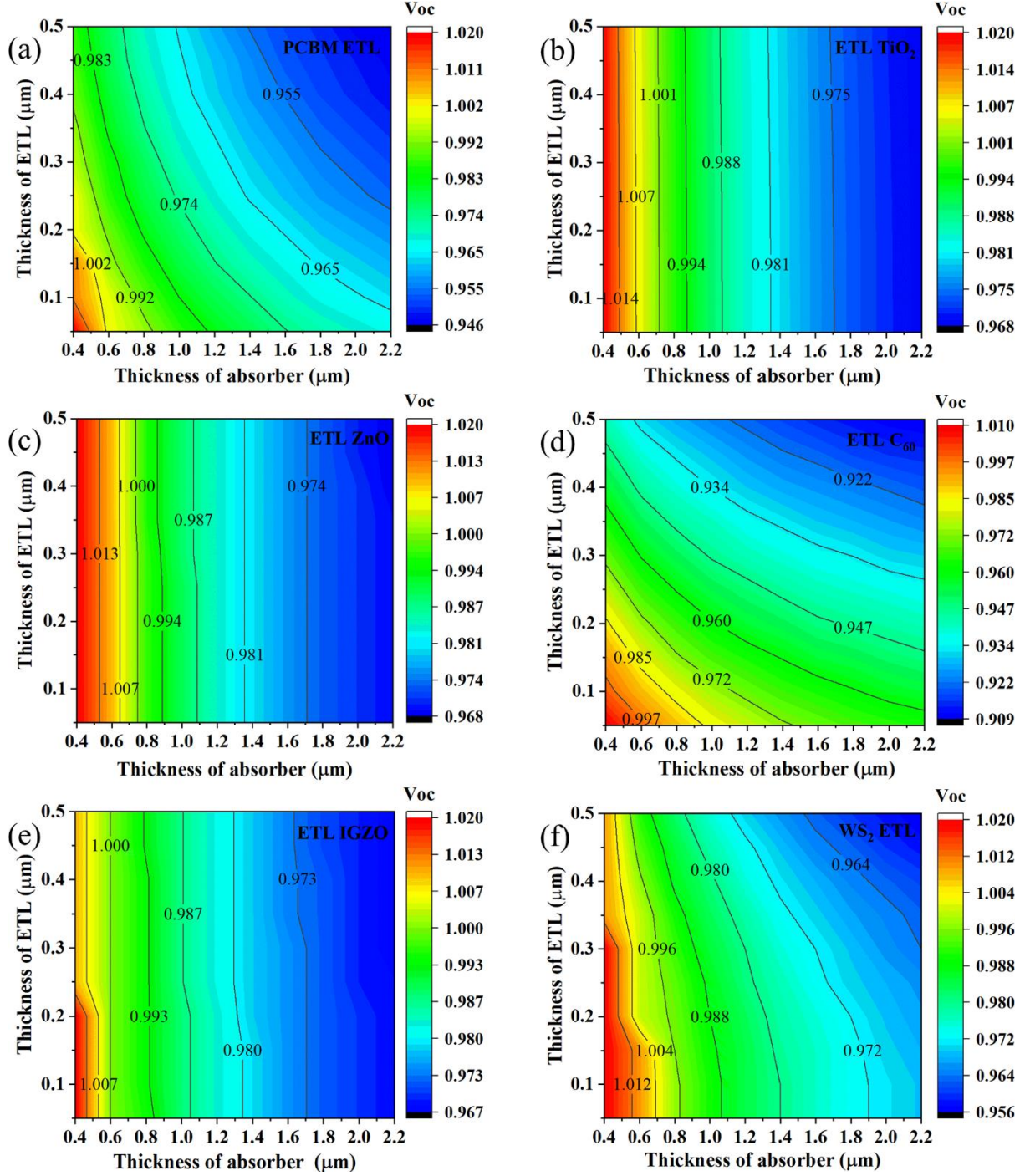


Figure 5: Contour mapping of V_{OC} with respect to the thickness of CsPbI_3 absorber and (a) C_{60} , (b) IGZO, (c) PCBM, (d) TiO_2 , (e) WS_2 , (f) ZnO ETLs, respectively.

The contour maps of the projected J_{SC} , V_{OC} , FF , and efficiency with respect to the varying ETL thickness (50 nm to 500 nm) and absorber thickness (400 nm to 2200 nm) have been shown in **Figures (5-8)** for the CsPbI_3 -based PSCs. In **Figure 5**, when the absorber and ETL thickness was around 400 nm and 50 nm, respectively, the PSCs with PCBM, TiO_2 , ZnO, IGZO, and WS_2 ETLs showed the maximum V_{OC} of 1.02 V, while the PSC with C_{60} ETL showed the maximum V_{OC} of 1.01 V. With the increase of absorber and ETL thickness, the V_{OC} of each device declined because of the rise of the reverse saturation current due to the presence of a thicker absorber and the partial absorption of light by a thicker ETL. Among all the devices, the lowest V_{OC} of 0.909 V was found for the PSC with C_{60} ETL when the absorber and ETL thickness was 2200 nm and 500 nm, respectively.

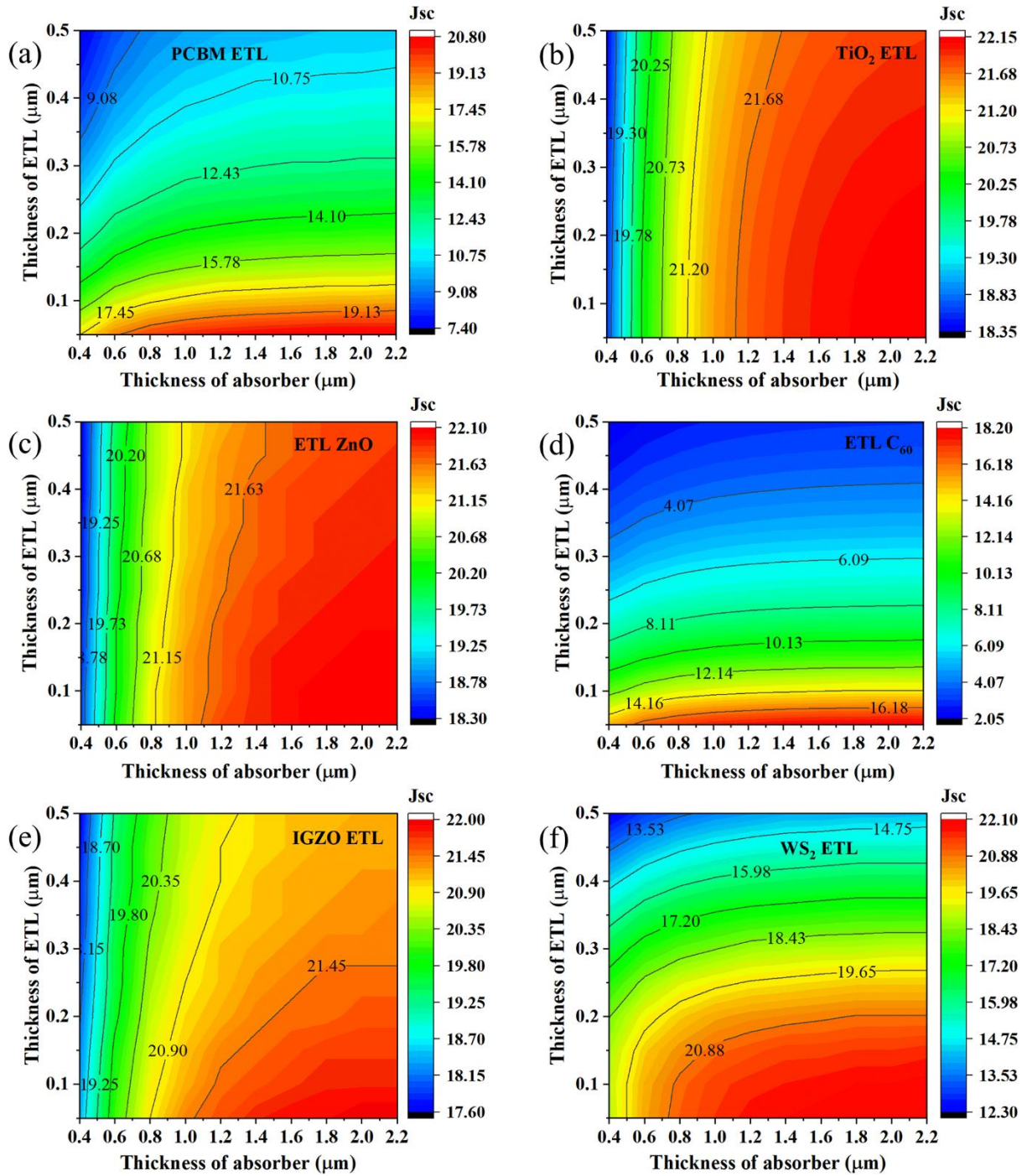


Figure 6. Contour mapping of J_{SC} with respect to the thickness of CsPbI_3 absorber and (a) C_{60} , (b) IGZO, (c) PCBM, (d) TiO_2 , (e) WS_2 , (f) ZnO ETLs, respectively.

In the case of the J_{SC} (**Figure 6**), the PSC with TiO_2 ETL showed a maximum value of 22.15 mA/cm^2 when absorber and ETL thickness was ≥ 1800 nm and ≤ 250 nm, respectively. The PSCs with ZnO and WS_2 ETLs showed the maximum J_{SC} values of 22.10 mA/cm^2 when the absorber and ETL thickness was ≥ 1400 nm and ≤ 150 nm, respectively. Besides, the PSCs with IGZO, PCBM, and C_{60} ETLs exhibited the maximum J_{SC} values of 22.00, 20.80, and 18.20 mA/cm^2 , respectively, when the absorber and ETL thickness was between 1600-2200 nm and 50-100 nm, respectively. Generally, for each device, the J_{SC} increased with the increment of absorber thickness due to the rise of spectral response at longer wavelengths, while the enhancement of ETL thickness lowered the J_{SC} due to the partial absorption of light.

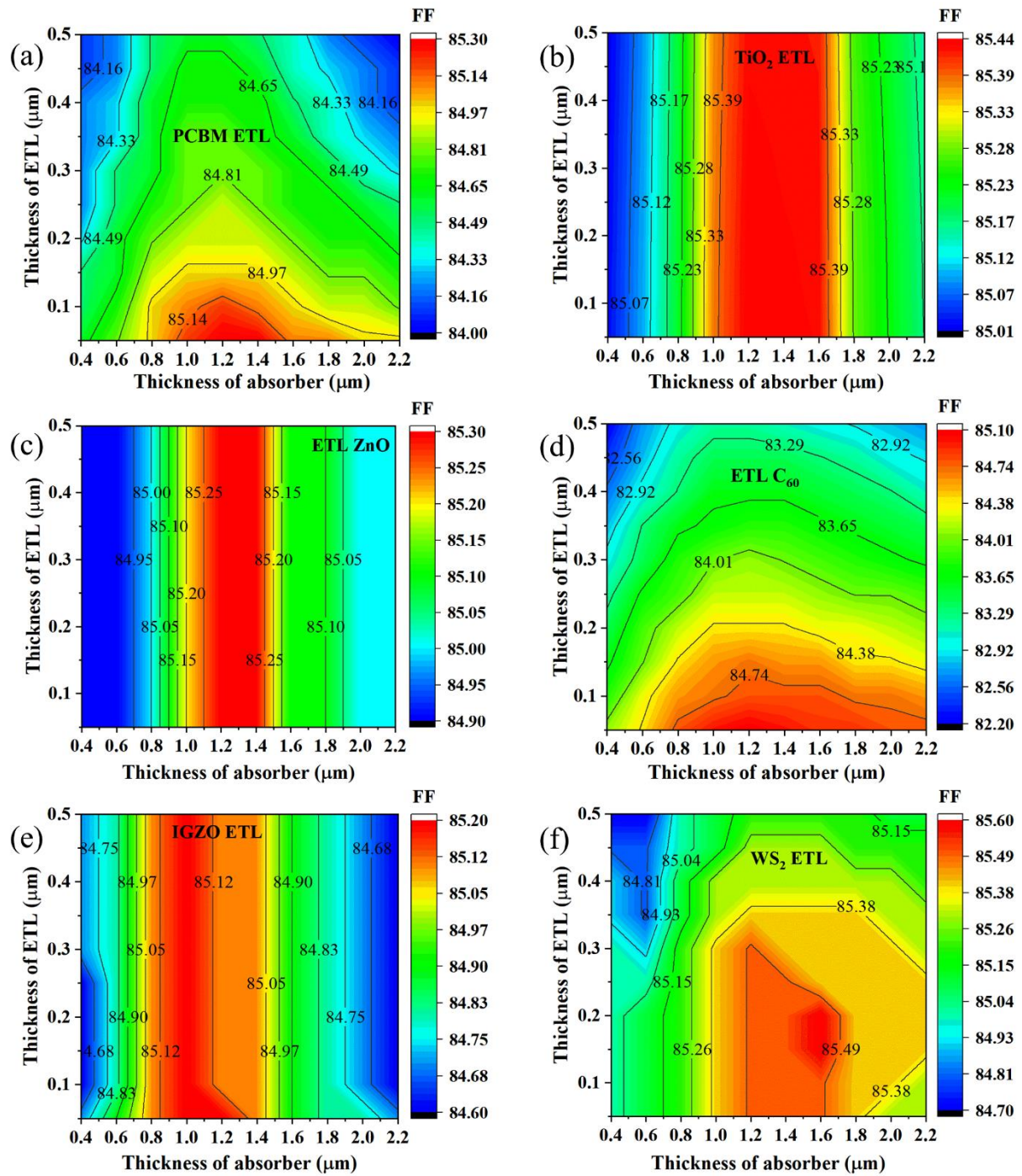


Figure 7: Contour mapping of FF with respect to the thickness of CsPbI_3 absorber and (a) C_{60} , (b) IGZO, (c) PCBM, (d) TiO_2 , (e) WS_2 , (f) ZnO ETLs, respectively.

In **Figure 7**, among all the CsPbI_3 -based PSCs, the WS_2 ETL showed the maximum FF of 85.65% between 1400-1600 nm and 100-200 nm of absorber and ETL thickness, respectively. For the TiO_2 ETL, a more stable FF of 85.44% was found when the absorber thickness was between 1000-1600 nm, and the ETL thickness was between 100-400 nm. For the ETLs like PCBM and ZnO, a similar FF of 85.30% was obtained while the absorber thickness ranged from 1000 nm to 1400 nm, and the ETL thickness was ≤ 200 nm. The PSC with C_{60} ETL exhibited the minimum FF of about 85.10% between 1000-1400 nm and 50-100 nm of absorber and ETL thickness, respectively.

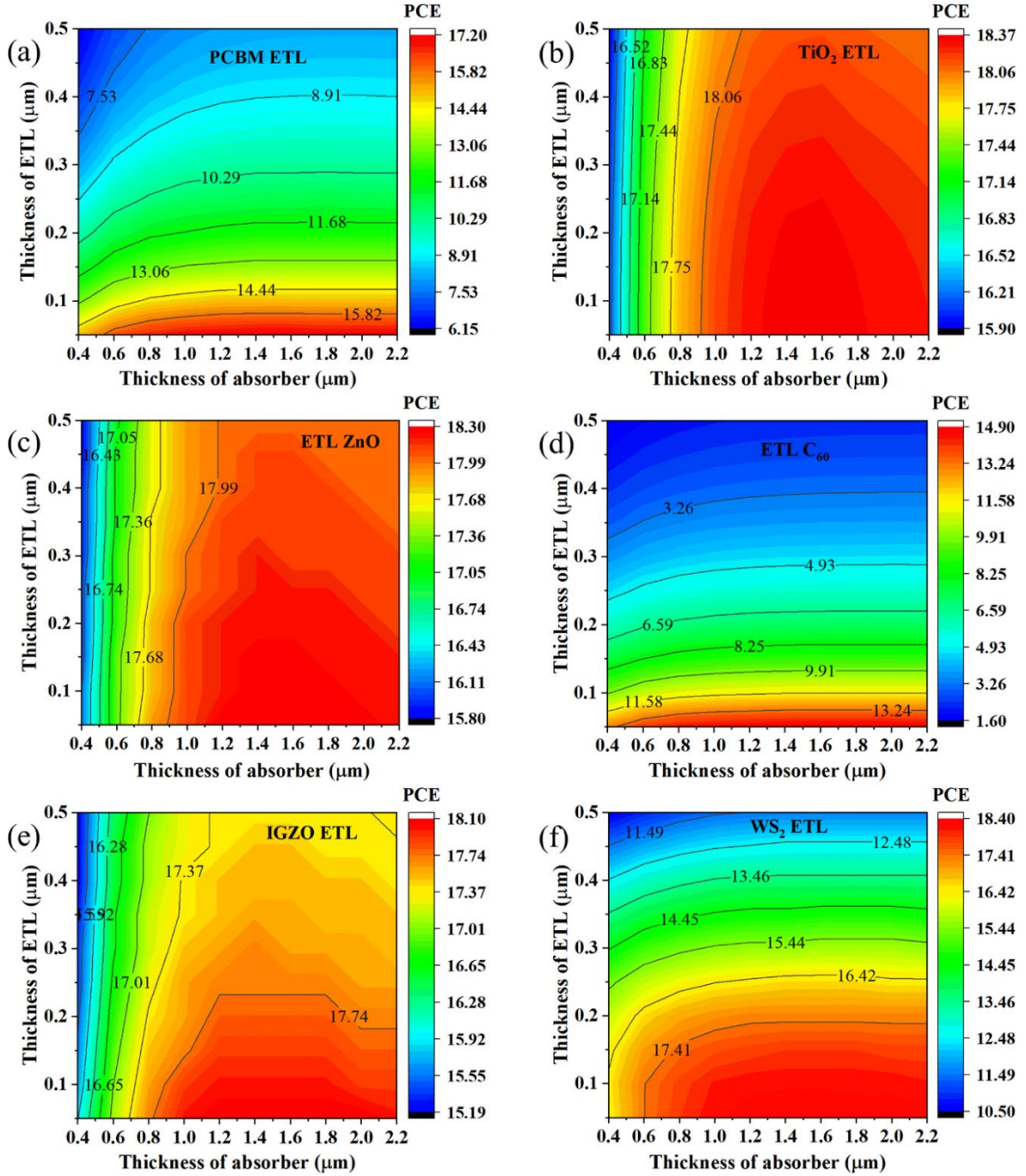


Figure 8: Contour mapping of PCE with respect to the thickness of CsPbI₃ absorber and (a) C₆₀, (b) IGZO, (c) PCBM, (d) TiO₂, (e) WS₂, (f) ZnO ETLs, respectively.

In **Figure 8**, among all the devices, the PSC with WS₂ ETL showed the highest efficiency of 18.40% between 1000-2000 nm absorber thickness and 50-100 nm ETL thickness. However, the devices with TiO₂ and ZnO ETLs also showed a good and consistent PCE of 18.37% and 18.30%, respectively, between 1200-2000 nm absorber thickness and 100-250 nm ETL thickness. In comparison with other devices, the PSC with C₆₀ ETL showed the lowest PCE of 14.90% with an absorber thickness between 1400 nm to 1600 nm and an ETL thickness of around 50 nm. As the PCE is a function of J_{SC} , V_{OC} , and FF parameters, with the increment of absorber and ETL thickness, the PV performance increased up to a certain range depending on the absorber and ETL material of the PSC parallel to the previous study⁸⁰.

3.2.5 Effect of series resistance

Figure 9 represents the effect of series resistance (R_S) in the ranges of 0-6 $\Omega\text{-cm}^2$ on the performance of ITO/ETL/CsPbI₃/CBTS/Au structure, whereas the shunt resistance (R_{SH}) was kept constant at $10^5 \Omega\text{-cm}^2$. From the figures, it could be identified how the variation of R_S affected the V_{OC} , J_{SC} , FF , and PCE . With the increasing R_S from 0-6 $\Omega\text{-cm}^2$, the V_{OC} increased marginally for all the studied devices, while the J_{SC} of every device was almost unchanged. On the other hand, both the FF and PCE decreased significantly by 11.02% and 2.24% on average (in magnitude), respectively, with the increment of R_S for each device. As a non-ohmic contact in a PSC shows a high R_S , the highly conductive ITO layer rarely induces any R_S ⁸¹. The R_S in a solar cell is made up of multiple resistances, including the resistance at the interface between semiconductors and metal contacts. Even though there is no net flow of current through the R_S , it might sometimes affect the V_{OC} ⁵⁰. If the R_S is raised, there is a significant reduction in the FF , which also decreases the PCE because of the higher power loss²⁴. For this reason, with the increment of R_S , the FF and PCE decreased in this work.

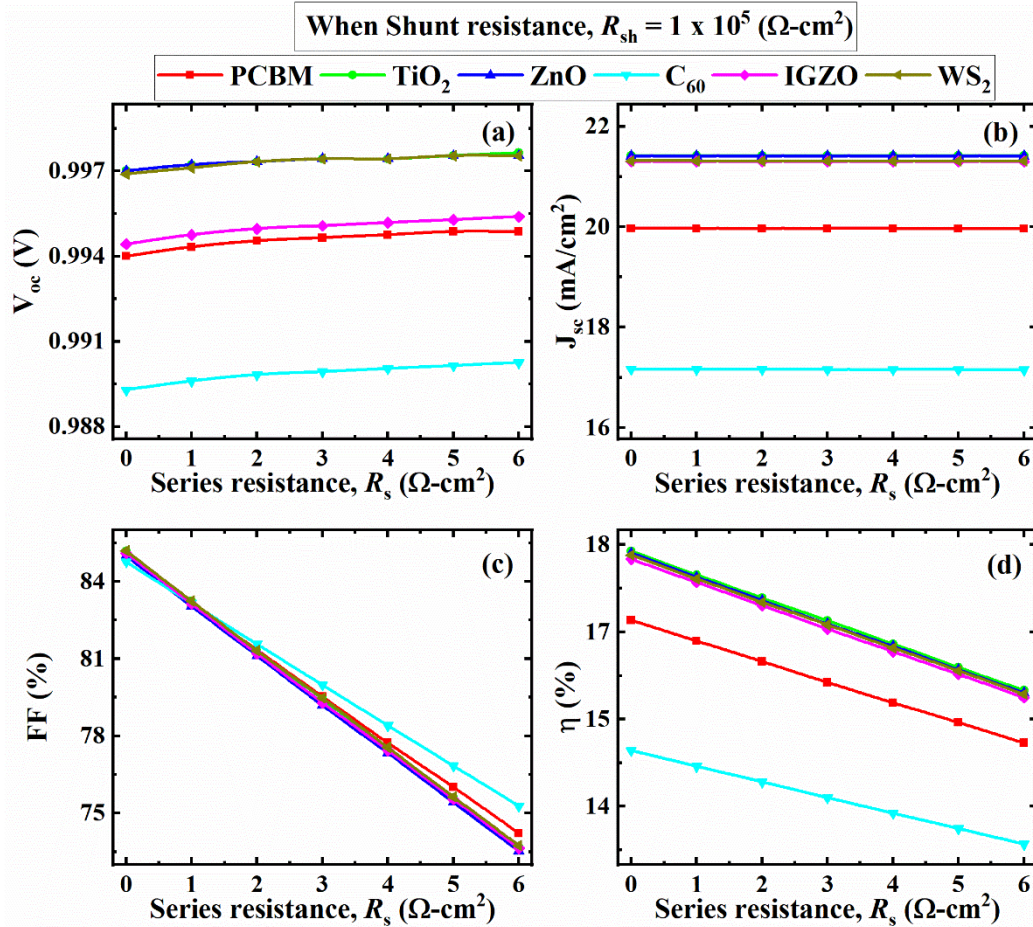


Figure 9. Effect of series resistance (R_S) on (a) V_{OC} , (b) J_{SC} , (c) FF , and (d) PCE when $R_{SH} = 10^5 \Omega\text{-cm}^2$.

3.2.6 Effect of shunt resistance

Figure 10 illustrates the effect of the alteration in shunt resistance (R_{SH}) in the ranges of $10 \Omega\text{-cm}^2$ to $10^7 \Omega\text{-cm}^2$ on the V_{OC} , J_{SC} , FF , and PCE of each device, while the R_S remained constant at $0.5 \Omega\text{-cm}^2$. The V_{OC} and J_{SC} increased up to $10^2 \Omega\text{-cm}^2$ R_{SH} for each of the six studied devices. After that, they were unchanged from $10^3 \Omega\text{-cm}^2$ to $10^7 \Omega\text{-cm}^2$. On the other hand, the FF and PCE increased by 55.51% and 15.16% on average (in magnitude), respectively, from 10 - $10^3 \Omega\text{-cm}^2$ R_{SH} values for each of the studied devices, and then, both became stable. The defects that occur during the manufacturing of the device give rise to R_{SH} ⁵⁶. The results of our research show that the R_{SH} can significantly improve the FF and PCE . A greater R_{SH} transforms the p-n junction into a route with low resistance so that the junction current may flow more easily, which can improve the device's performance^{50,56}.

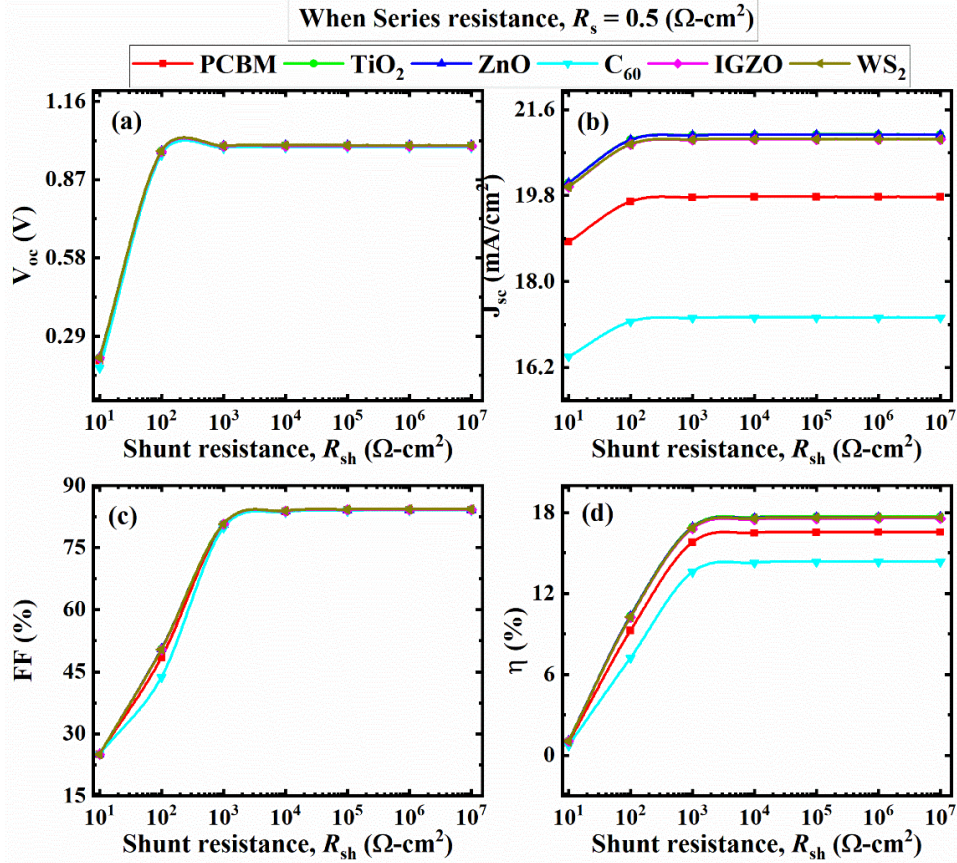


Figure 10. Effect of shunt resistance (R_{SH}) on (a) V_{OC} , (b) J_{SC} , (c) FF , and (d) PCE when $R_s = 0.5 \text{ } \Omega\text{-cm}^2$.

3.2.7 Effect of temperature

Figure S3 depicts the influence of the change of temperatures from 275 K to 450 K on the electrical outputs like V_{OC} , J_{SC} , FF , and PCE of the six devices. During the study, we noticed that the V_{OC} , FF , and PCE decreased with the increase of the temperature for every structure, whereas the J_{SC} changed slightly for every device. The steady drop in the device performance with a temperature rise is in line with the findings that were obtained before⁸². This could be a result of the defect density inside the layers increasing with temperature, causing an efficiency loss. In addition, when the temperature rises, the deformation stress also moves onward, which in turn, decreases the efficiency by 10.33% on average (in magnitude). The rising temperature influences the diffusion length, and as a consequence, the R_s rises, affecting the FF and efficiency of the device^{83,84}.

3.2.8 Capacitance and Mott-Schottky analysis

Figures 11(a) and **(b)** demonstrate the variation in capacitance and Mott-Schottky (MS) values, respectively, when the voltage was enhanced from -0.5 V to 0.8 V for the six devices, and the frequency was fixed at 1 MHz. The capacitance progressively rose with the applied voltage and quickly improved at the higher voltages before reaching its maximum value. **Figure 11(a)** illustrates that all the device was depleted at zero bias, whereas when a forward bias of about 0.5 V was introduced, the depletion width declined to a value that was roughly equivalent to the absorber thickness. Therefore, as the forward bias voltage was increased, the capacitance improved as well and behaved following the MS relationship. It has previously been observed that at low voltages, the current is drastically lower than the saturation current, but at voltage spikes, the current is only allowed to reach the contact's saturation current⁸⁵. On the other hand, the MS is a widely used and reliable tool for determining a device's built-in potential (V_{bi}), which is the contrast observed between the functions of electrode operation and doping level. The MS theory is primarily based on the characteristics of the p-n junction, where the x-axis intercept typically represents the V_{bi} of the semiconductor devices. The slope of $1/C^2 \text{ (V)}$ interprets as the concentration of inhabited trapping centers, even though the results are lower than anticipated due to the different electrode work functions⁸⁶. For every device in this work, with the increase of applied voltage values, the MS values got lowered, which is similar to the previous studies^{86,87}.

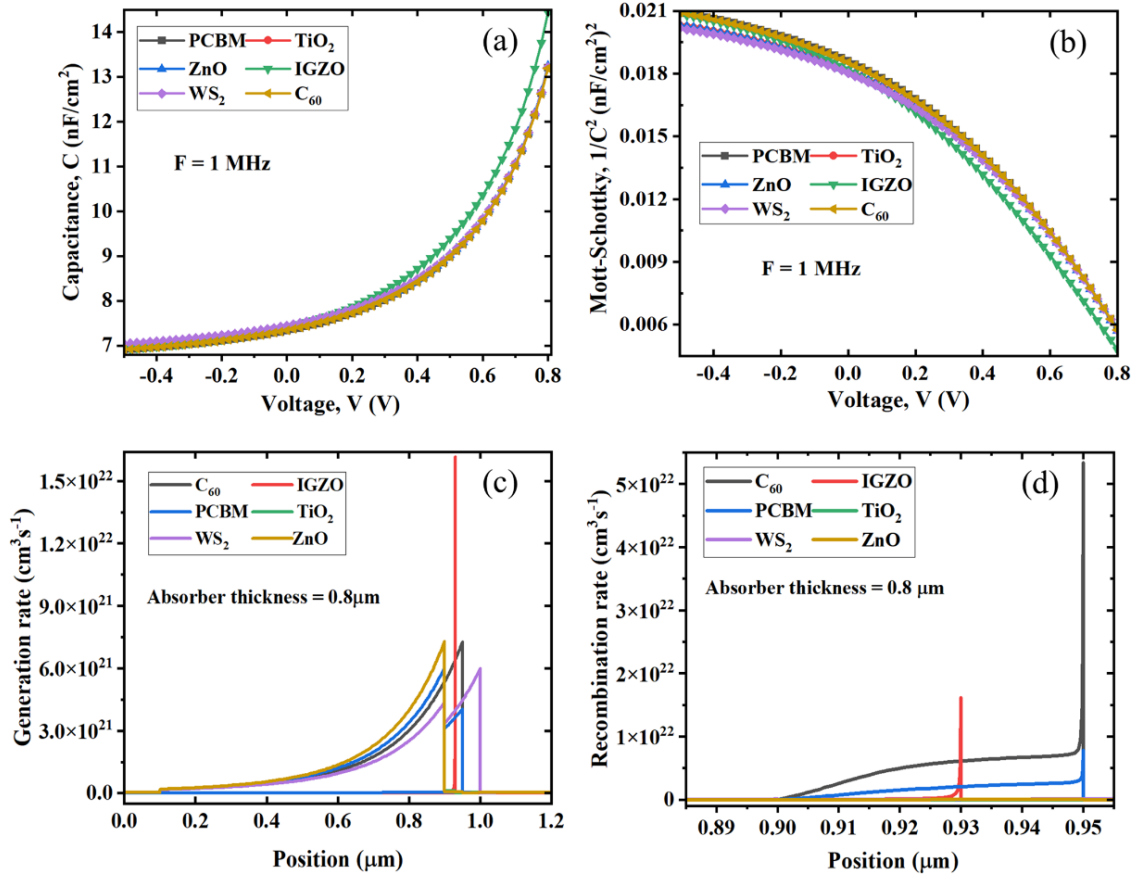


Figure 11: Analysis of (a) capacitance (C), (b) Mott-Schottky ($1/C^2$), (c) generation rate, and (d) recombination rate for CsPbI₃-based PSCs with different ETLs.

3.2.9 Generation and recombination rate analysis

Figures 11(c) and (d), respectively, demonstrate the carrier generation and recombination rate concerning the position of the CsPbI₃-based PSCs. For all PSCs, the electron-hole pairs are formed during the carrier generation stage when an electron is excited from the valence band to the conduction band, leaving a hole in the valence band. The carrier formation is driven by the release of electrons and holes of these PSCs. Usually, the maximum generation rates for the devices were found when the position was in the 0.9 μm to 1.0 μm range, while IGZO ETL showed the maximum generation rate. Because at this range, the generation rate corresponding to the maximum number of electrons generated at that particular position in the device due to the increased absorption of photons in comparison with other positions. The creation of electron-hole pairs, $G(x)$ is computed by SCAPS-1D using the incoming photon flux, $N_{\text{phot}}(\lambda, x)$, and **Eq. (11)** illustrates the value of $G(x)$ in terms of this photon flux for every spectrum and each region:

$$G(\lambda, x) = \alpha(\lambda, x) \cdot N_{\text{phot}}(\lambda, x) \quad (11)$$

On the contrary, the recombination rate is the opposite of the generation rate, in which the electrons and holes of the conduction band get united as well as eliminated. The lifespan and density of the charge carrier affect the rate of recombination in the PSCs. Moreover, the defect states that occur within each layer of PSC also influence electron-hole recombination. Similar to the generation rate, the maximum recombination rates for the devices were observed when the position was in the 0.9 μm to 1.0 μm range, where C₆₀ ETL showed the maximum recombination rate. Because at this particular range, in comparison with other positions, more electrons in the conduction band surpassed the energy gap and reached the valence band to become stable and occupy the position of a hole in the valence band. The electron-hole recombination profile within the devices is subsequently impacted by the energy levels that are produced at that point, and the grain boundaries and imperfections enable the recombination rate distribution to be non-uniform in the PSCs⁸⁷.

3.2.10 J - V and QE characteristics

Figure 12(a) shows the J - V characteristics for the six best configurations of this work. It was observed that the TiO_2 , ZnO , and WS_2 as the ETL showed better J - V characteristics for the PSC in comparison with other ETLs, while the C_{60} ETL showed the worst J - V characteristics.

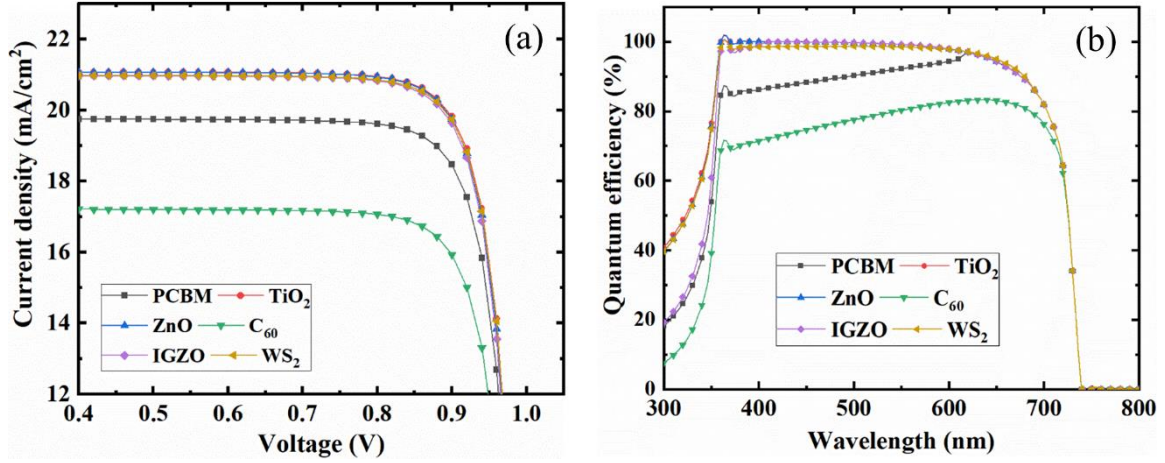


Figure 12. Effect of (a) J - V , and (b) QE for six studied devices.

Figure 12(b) illustrates how the wavelength and QE are interrelated for the six best devices of this study. The QE depends on the wavelength of the light (λ). It is the ratio of the number of charge carriers made by a solar cell to the number of photons that hit that cell⁵⁰. The QE usually gets better as the absorber thickness gets higher as a thicker absorber can absorb more photons⁸². Similar to the J - V characteristics, when the TiO_2 , ZnO , and WS_2 were utilized as the ETL, the PSC showed better QE characteristics, whereas the C_{60} as the ETL showed the poorest QE characteristics.

3.3 Comparison with wxAMPS results and previous work

3.3.1 Comparison between SCAPS-1D and wxAMPS results

The findings of the SCAPS-1D (Table 4) were also validated through the simulations in wxAMPS (version 2.0) software. Both software conducted simulations with an absorber thickness, absorber acceptor density, and defect density of 800 nm, 10^{15} cm^{-3} , and 10^{15} cm^{-3} , respectively, to identify the change in PV characteristics among all 6 optimized devices. Similar to the previous SCAPS-1D simulations of this work, all the device simulations with wxAMPS were also run at an operating temperature of 300 K with an AM1.5G sun spectrum. A comparison between the SCAPS-1D and wxAMPS software simulation results has been enlisted in Table 5. The difference in results between the two simulation tools was satisfactory, and these kinds of findings were quite similar to previous studies^{47,48,88}.

Table 5: Comparison between SCAPS-1D and wxAMPS software simulation results.

Device structure	Software	V_{oc} (V)	J_{sc} (mA/cm ²)	FF (%)	PCE (%)
ITO/PCBM/CsPbI ₃ /CBTS/Au	SCAPS-1D	0.994	19.77	85.04	16.71
	wxAMPS	1.000	21.00	84.51	17.77
ITO/TiO ₂ /CsPbI ₃ /CBTS/Au	SCAPS-1D	0.997	21.07	85.21	17.90
	wxAMPS	1.010	22.97	85.23	19.75
ITO/ZnO/CsPbI ₃ /CBTS/Au	SCAPS-1D	0.997	21.07	85.03	17.86
	wxAMPS	1.000	21.94	84.66	18.63
ITO/C ₆₀ /CsPbI ₃ /CBTS/Au	SCAPS-1D	0.989	17.25	84.80	14.47
	wxAMPS	1.000	21.22	84.54	17.97
ITO/IGZO/CsPbI ₃ /CBTS/Au	SCAPS-1D	0.995	20.98	85.13	17.76
	wxAMPS	1.000	22.82	84.65	19.36
ITO/WS ₂ /CsPbI ₃ /CBTS/Au	SCAPS-1D	0.997	20.98	85.22	17.82
	wxAMPS	1.000	21.05	84.55	17.82

3.3.2 Comparison of SCAPS-1D results with previous work

Table 6 shows the comparison between the recent experimental and theoretical works on CsPbI₃-based PSC with our study. All the previous experimental works have been done by the change of strategies like ionic incorporation, metastable phase, reducing crystal size/dimensional engineering, or steric hindrance to overcome the drawbacks of CsPbI₃^{22,89,98–102,90–97}. In those experiments, the PCE reached up to 18.40%⁹⁰ with these modifications. However, there is a lack of theoretical study available regarding the performance enhancement of the CsPbI₃ absorber, and the maximum PCE obtained via simulation is 15.6%²⁴. We also noticed that most experiments used TiO₂, PTAA, and ZnO as the ETL, but there were variations in HTL and back contact metal. But in many cases, the results were not up to expectations. That's why we had gone through all these simulations to find out the best combinations to achieve an excellent performance.

Table 6. The comparison of PV parameters of CsPbI₃-based solar cells.

Type	Device structure	Voc (V)	Jsc (mA/cm ²)	FF (%)	PCE (%)	Year	Ref.
E	FTO/TiO ₂ /CsPbI ₃ /PTAA/Au	1.084	19.72	75.70	16.07	2019	89
E	FTO/TiO ₂ /CsPbI ₃ /PTAA/Au	1.090	20.34	77.00	17.03	2017	91
E	FTO/TiO ₂ /CsPbI ₃ /P3HT/Au	1.040	16.53	65.70	11.30	2018	92
E	FTO/TiO ₂ /CsPbI ₃ /PTAA/Au	1.059	18.95	75.10	15.07	2018	22
E	FTO/TiO ₂ /CsPbI ₃ /C	0.790	18.50	65.00	9.50	2018	93
E	ITO/PTAA/CsPbI ₃ /C ₆₀ /BCP/Cu	0.960	17.50	73.00	12.50	2019	94
E	FTO/TiO ₂ /CsPbI ₃ /P3HT/Au	1.020	17.40	79.40	14.10	2018	95
E	ITO/PTAA/CsPbI ₃ /BCP/Cu	1.120	17.10	70.01	13.40	2019	96
E	FTO/TiO ₂ /CsPbI ₃ /Spiro/Ag	1.110	20.23	82.00	18.40	2019	90
E	FTO/TiO ₂ /CsPbI ₃ /Spiro/MoO _x /Al	0.990	13.47	65.00	10.77	2016	97
E	FTO/TiO ₂ /CsPbI ₃ /Spiro/Au	1.110	14.88	65.00	10.74	2018	98
E	FTO/TiO ₂ /CsPbI ₃ /Spiro/Ag	0.660	11.92	52.47	4.13	2016	99
E	FTO/TiO ₂ /CsPbI ₃ /PTAA/Au	0.993	19.51	70.46	13.65	2019	100
E	FTO/TiO ₂ /CsPbI ₃ /Spiro/Au	1.110	14.80	74.00	12.15	2019	102
E	FTO/TiO ₂ /CsPbI ₃ /PTAA/Au	1.204	15.25	78.70	14.45	2018	101
T	FTO/ZnO/CsPbI ₃ /CuSbS ₂ /Se	1.103	22.59	62.64	15.60	2021	24
T	ITO/PCBM/CsPbI ₃ /CBTS/Au	0.994	19.77	85.04	16.71	2022	*
T	ITO/TiO ₂ /CsPbI ₃ /CBTS/Au	0.997	21.07	85.21	17.90	2022	*
T	ITO/ZnO/CsPbI ₃ /CBTS/Au	0.997	21.07	85.03	17.86	2022	*
T	ITO/C ₆₀ /CsPbI ₃ /CBTS/Au	0.989	17.25	84.80	14.47	2022	*
T	ITO/IGZO/CsPbI ₃ /CBTS/Au	0.995	20.98	85.13	17.76	2022	*
T	ITO/WS ₂ /CsPbI ₃ /CBTS/Au	0.997	20.98	85.22	17.82	2022	*

Note: E = Experimental, T = Theoretical, *This work

4 Conclusion

In this study, first-principle DFT simulations were done to examine the structural and optical characteristics, as well as electronic properties of the CsPbI₃ absorber, including electron charge density, Fermi surface, DOS, and band structure. The CsPbI₃ absorber's computed bandgap using DFT was 1.483 eV. Additionally, both the charge density map and DOS demonstrated that the Pb-5d orbital is the primary source of contribution for the Pb atom. The observation of a surface that resembles a Fermi surface for holes and electrons indicates that the CsPbI₃ perovskite is multiband in nature. Furthermore, SCAPS-1D was used to perform numerical simulation and optimization of CsPbI₃-based PSC. A diverse set of HTLs and ETLs were explored to find the optimal combination from 96 device structures. From the optimization, CBTS HTL exhibited superior performance with PCBM, TiO₂, ZnO, C₆₀, IGZO, and WS₂ ETLs in comparison to other HTLs that were studied. We elected the six best devices to find the effect of absorber and ETL thickness, R_s , R_{SH} , and temperature on their performance along with their

corresponding capacitance, Mott-Schottky, generation rate, recombination rate, $J-V$, and QE characteristics. Among all six devices, the PSC with TiO_2 ETL and CBTS HTL showed the highest PCE of 17.9%. Moreover, the TiO_2 and ZnO ETLs showed the best performance during the absorber and ETL thickness variation. Due to the increment of R_S and temperature, the performance of all six devices decreased, while the performance of each device increased with the increasing R_{SH} . The $C-V$ characteristics of the device with IGZO ETL were slightly different compared to other devices, whereas among all the devices, the generation and recombination rates of the device with IGZO ETL were better. When the TiO_2 , ZnO , and WS_2 were utilized as the ETL, the PSC showed better QE and $J-V$ characteristics, whereas the C_{60} as the ETL showed the worst QE and $J-V$ characteristics. Also, wxAMPS numerical simulations were carried out to compare with the SCAPS-1D simulation results. Finally, this simulation study assisted in finding an optimum ETL/ $CsPbI_3$ /HTL combination as a guide to experimentally fabricate a low-cost, stable, and highly efficient $CsPbI_3$ -based PSC because it is impractical to experimentally investigate all probable combinations. The incorporation of machine learning into this work can be recommended to find a better combination for $CsPbI_3$ -based PSC in the future.

Supporting Information

Energy level alignment of studied ITO, 9 ETLs, $CsPbI_3$, and 12 HTLs (Figure S1); Best optimized structures of $CsPbI_3$ -based PSC with CBTS as the HTL and PCBM, TiO_2 , ZnO , C_{60} , IGZO, and WS_2 as ETLs (Figure S2); Effect of the variation in temperature from 275 K to 475 K on V_{OC} , J_{SC} , FF , and PCE (Figure S3).

Data availability

The raw/processed data required to reproduce these findings cannot be shared at this time as the data also forms part of an ongoing study.

Declaration of interests

The authors declare that they have no known competing financial interests or personal relationships that could have appeared to influence the work reported in this paper.

Funding Sources

This research did not receive any specific grant from funding agencies in the public, commercial, or not-for-profit sectors.

Acknowledgments

The SCAPS-1D program was kindly provided by Dr. M. Burgelman of the University of Gent in Belgium. The authors would like to express their gratitude to him. They would also like to thank Professor A. Rockett and Dr. Yiming Liu from UIUC, as well as Professor Fonash from Penn State University, for their contributions to the wxAMPS program.

References

- (1) Gao, P.; Grätzel, M.; Nazeeruddin, M. K. Organohalide Lead Perovskites for Photovoltaic Applications. *Energy Environ. Sci.* **2014**, *7* (8), 2448–2463. <https://doi.org/10.1039/C4EE00942H>.
- (2) Lee, M. M.; Teuscher, J.; Miyasaka, T.; Murakami, T. N.; Snaith, H. J. Efficient Hybrid Solar Cells Based on Meso-Superstructured Organometal Halide Perovskites. *Science* (80-.). **2012**, *338* (6107), 643–647. <https://doi.org/10.1126/science.1228604>.
- (3) Conings, B.; Drijkoningen, J.; Gauquelin, N.; Babayigit, A.; D'Haen, J.; D'Olieslaeger, L.; Ethirajan, A.; Verbeeck, J.; Manca, J.; Mosconi, E.; Angelis, F. De; Boyen, H.-G. Intrinsic Thermal Instability of Methylammonium Lead Trihalide Perovskite. *Adv. Energy Mater.* **2015**, *5* (15), 1500477. <https://doi.org/10.1002/aenm.201500477>.
- (4) Jeong, J.; Kim, M.; Seo, J.; Lu, H.; Ahlawat, P.; Mishra, A.; Yang, Y.; Hope, M. A.; Eickemeyer, F. T.; Kim, M.; Yoon, Y. J.; Choi, I. W.; Darwich, B. P.; Choi, S. J.; Jo, Y.; Lee, J. H.; Walker, B.; Zakeeruddin, S. M.; Emsley, L.; Rothlisberger, U.; Hagfeldt, A.; Kim, D. S.; Grätzel, M.; Kim, J. Y. Pseudo-Halide

- Anion Engineering for α -FAPbI₃ Perovskite Solar Cells. *Nature* **2021**, *592* (7854), 381–385. <https://doi.org/10.1038/s41586-021-03406-5>.
- (5) Ehrler, B.; Alarcón-Lladó, E.; Tabernig, S. W.; Veeken, T.; Garnett, E. C.; Polman, A. Photovoltaics Reaching for the Shockley–Queisser Limit. *ACS Energy Lett.* **2020**, *5* (9), 3029–3033. <https://doi.org/10.1021/acscenergylett.0c01790>.
 - (6) Hossain, M. K.; Raihan, G. A.; Akbar, M. A.; Kabir Rubel, M. H.; Ahmed, M. H.; Khan, M. I.; Hossain, S.; Sen, S. K.; Jalal, M. I. E.; El-Denglawey, A. Current Applications and Future Potential of Rare Earth Oxides in Sustainable Nuclear, Radiation, and Energy Devices: A Review. *ACS Appl. Electron. Mater.* **2022**, *4* (7), 3327–3353. <https://doi.org/10.1021/acsaelm.2c00069>.
 - (7) Hossain, M. K.; Hasan, S. M. K.; Hossain, M. I.; Das, R. C.; Bencherif, H.; Rubel, M. H. K.; Rahman, M. F.; Emrose, T.; Hashizume, K. A Review of Applications, Prospects, and Challenges of Proton-Conducting Zirconates in Electrochemical Hydrogen Devices. *Nanomaterials* **2022**, *12* (20), 3581. <https://doi.org/10.3390/nano12203581>.
 - (8) Hossain, M. K.; Rubel, M. H. K.; Akbar, M. A.; Ahmed, M. H.; Haque, N.; Rahman, M. F.; Hossain, J.; Hossain, K. M. A Review on Recent Applications and Future Prospects of Rare Earth Oxides in Corrosion and Thermal Barrier Coatings, Catalysts, Tribological, and Environmental Sectors. *Ceram. Int.* **2022**. <https://doi.org/10.1016/j.ceramint.2022.07.220>.
 - (9) Kulbak, M.; Cahen, D.; Hodes, G. How Important Is the Organic Part of Lead Halide Perovskite Photovoltaic Cells? Efficient CsPbBr₃ Cells. *J. Phys. Chem. Lett.* **2015**, *6* (13), 2452–2456. <https://doi.org/10.1021/acs.jpcclett.5b00968>.
 - (10) Burschka, J.; Pellet, N.; Moon, S.-J.; Humphry-Baker, R.; Gao, P.; Nazeeruddin, M. K.; Grätzel, M. Sequential Deposition as a Route to High-Performance Perovskite-Sensitized Solar Cells. *Nature* **2013**, *499* (7458), 316–319. <https://doi.org/10.1038/nature12340>.
 - (11) Hossain, M. K.; Pervez, M. F.; Tayyaba, S.; Uddin, M. J.; Mortuza, A. A.; Mia, M. N. H.; Manir, M. S.; Karim, M. R.; Khan, M. A. Efficiency Enhancement of Natural Dye Sensitized Solar Cell by Optimizing Electrode Fabrication Parameters. *Mater. Sci.* **2017**, *35* (4), 816–823. <https://doi.org/10.1515/msp-2017-0086>.
 - (12) Hossain, M. K.; Rahman, M. T.; Basher, M. K.; Afzal, M. J.; Bashar, M. S. Impact of Ionizing Radiation Doses on Nanocrystalline TiO₂ Layer in DSSC's Photoanode Film. *Results Phys.* **2018**, *11*, 1172–1181. <https://doi.org/10.1016/j.rinp.2018.10.006>.
 - (13) Basher, M. K.; Uddin, M. J.; Hossain, M. K.; Akand, M. A. R.; Biswas, S.; Mia, M. N. H.; Shorowordi, K. M. Effect of Doping Profile on Sheet Resistance and Contact Resistance of Monocrystalline Silicon Solar Cells. *Mater. Res. Express* **2019**, *6* (8), 085510. <https://doi.org/10.1088/2053-1591/ab1e8c>.
 - (14) Basher, M. K.; Mishan, R.; Biswas, S.; Hossain, M. K.; Akand, M. A. R.; Matin, M. A. Study and Analysis the Cu Nanoparticle Assisted Texturization Forming Low Reflective Silicon Surface for Solar Cell Application. *AIP Adv.* **2019**, *9* (7), 075118. <https://doi.org/10.1063/1.5109003>.
 - (15) Kojima, A.; Teshima, K.; Shirai, Y.; Miyasaka, T. Organometal Halide Perovskites as Visible-Light Sensitizers for Photovoltaic Cells. *J. Am. Chem. Soc.* **2009**, *131* (17), 6050–6051. <https://doi.org/10.1021/ja809598r>.
 - (16) *Best Research-Cell Efficiency Chart.*
 - (17) Stoumpos, C. C.; Malliakas, C. D.; Kanatzidis, M. G. Semiconducting Tin and Lead Iodide Perovskites with Organic Cations: Phase Transitions, High Mobilities, and Near-Infrared Photoluminescent Properties. *Inorg. Chem.* **2013**, *52* (15), 9019–9038. <https://doi.org/10.1021/ic401215x>.
 - (18) Bencherif, H.; Meddour, F.; Elshorbagy, M. H.; Hossain, M. K.; Cuadrado, A.; Abdi, M. A.; Bendib, T.; Kouda, S.; Alda, J. Performance Enhancement of (FAPbI₃)_{1-x}(MAPbBr₃)_x Perovskite Solar Cell with an Optimized Design. *Micro and Nanostructures* **2022**, *171*, 207403. <https://doi.org/10.1016/j.micrna.2022.207403>.
 - (19) Hu, Y.; Bai, F.; Liu, X.; Ji, Q.; Miao, X.; Qiu, T.; Zhang, S. Bismuth Incorporation Stabilized α -CsPbI₃ for Fully Inorganic Perovskite Solar Cells. *ACS Energy Lett.* **2017**, *2* (10), 2219–2227. <https://doi.org/10.1021/acscenergylett.7b00508>.
 - (20) Zhang, T.; Dar, M. I.; Li, G.; Xu, F.; Guo, N.; Grätzel, M.; Zhao, Y. Bication Lead Iodide 2D Perovskite Component to Stabilize Inorganic α -CsPbI₃ Perovskite Phase for High-Efficiency Solar Cells. *Sci. Adv.* **2017**, *3* (9). <https://doi.org/10.1126/sciadv.1700841>.
 - (21) Eperon, G. E.; Paternò, G. M.; Sutton, R. J.; Zampetti, A.; Haghighirad, A. A.; Cacialli, F.; Snaith, H. J.

- Inorganic Caesium Lead Iodide Perovskite Solar Cells. *J. Mater. Chem. A* **2015**, *3* (39), 19688–19695. <https://doi.org/10.1039/C5TA06398A>.
- (22) Wang, K.; Jin, Z.; Liang, L.; Bian, H.; Bai, D.; Wang, H.; Zhang, J.; Wang, Q.; Liu, S. All-Inorganic Cesium Lead Iodide Perovskite Solar Cells with Stabilized Efficiency beyond 15%. *Nat. Commun.* **2018**, *9* (1), 4544. <https://doi.org/10.1038/s41467-018-06915-6>.
 - (23) Jiang, Y.; Yuan, J.; Ni, Y.; Yang, J.; Wang, Y.; Jiu, T.; Yuan, M.; Chen, J. Reduced-Dimensional α -CsPbX₃ Perovskites for Efficient and Stable Photovoltaics. *Joule* **2018**, *2* (7), 1356–1368. <https://doi.org/10.1016/j.joule.2018.05.004>.
 - (24) Jayan K, D.; Sebastian, V.; Kurian, J. Simulation and Optimization Studies on CsPbI₃ Based Inorganic Perovskite Solar Cells. *Sol. Energy* **2021**, *221*, 99–108. <https://doi.org/10.1016/j.solener.2021.04.030>.
 - (25) Raoui, Y.; Ez-zahraouy, H.; Tahiri, N.; El, O.; Ahmad, S.; Kazim, S.; El Bounagui, O.; Ahmad, S.; Kazim, S. Performance Analysis of MAPbI₃ Based Perovskite Solar Cells Employing Diverse Charge Selective Contacts: Simulation Study. *Sol. Energy* **2019**, *193* (February), 948–955. <https://doi.org/10.1016/j.solener.2019.10.009>.
 - (26) Abdelaziz, S.; Zekry, A.; Shaker, A.; Abouelatta, M. Investigating the Performance of Formamidinium Tin-Based Perovskite Solar Cell by SCAPS Device Simulation. *Opt. Mater. (Amst)*. **2020**, *101* (February), 109738. <https://doi.org/10.1016/j.optmat.2020.109738>.
 - (27) Gan, Y.; Bi, X.; Liu, Y.; Qin, B.; Li, Q.; Jiang, Q.; Mo, P. Numerical Investigation Energy Conversion Performance of Tin-Based Perovskite Solar Cells Using Cell Capacitance Simulator. *Energies* **2020**, *13* (22), 5907. <https://doi.org/10.3390/en13225907>.
 - (28) Singla, A.; Pandey, R.; Sharma, R.; Madan, J.; Singh, K.; Yadav, V. K.; Chaujar, R. Numerical Simulation of CeO_x ETL Based Perovskite Solar Cell:- An Optimization Study for High Efficiency and Stability. In *2018 IEEE Electron Devices Kolkata Conference (EDKCON)*; IEEE, 2018; pp 278–282. <https://doi.org/10.1109/EDKCON.2018.8770401>.
 - (29) Lakhdar, N.; Hima, A. Electron Transport Material Effect on Performance of Perovskite Solar Cells Based on CH₃NH₃GeI₃. *Opt. Mater. (Amst)*. **2020**, *99* (November), 109517. <https://doi.org/10.1016/j.optmat.2019.109517>.
 - (30) Wang, Y.; Wan, J.; Ding, J.; Hu, J.; Wang, D. A Rutile TiO₂ Electron Transport Layer for the Enhancement of Charge Collection for Efficient Perovskite Solar Cells. *Angew. Chemie Int. Ed.* **2019**, *58* (28), 9414–9418. <https://doi.org/10.1002/anie.201902984>.
 - (31) Heo, J. H.; Han, H. J.; Kim, D.; Ahn, T. K.; Im, S. H. Hysteresis-Less Inverted CH₃NH₃PbI₃ Planar Perovskite Hybrid Solar Cells with 18.1% Power Conversion Efficiency. *Energy Environ. Sci.* **2015**, *8* (5), 1602–1608. <https://doi.org/10.1039/C5EE00120J>.
 - (32) Shi, X.; Ding, Y.; Zhou, S.; Zhang, B.; Cai, M.; Yao, J.; Hu, L.; Wu, J.; Dai, S.; Nazeeruddin, M. K. Enhanced Interfacial Binding and Electron Extraction Using Boron-Doped TiO₂ for Highly Efficient Hysteresis-Free Perovskite Solar Cells. *Adv. Sci.* **2019**, *6* (21), 1901213. <https://doi.org/10.1002/advs.201901213>.
 - (33) Zhu, L.; Shang, X.; Lei, K.; Wu, C.; Zheng, S.; Chen, C.; Song, H. Doping in Semiconductor Oxides-Based Electron Transport Materials for Perovskite Solar Cells Application. *Sol. RRL* **2021**, *5* (3), 2000605. <https://doi.org/10.1002/solr.202000605>.
 - (34) Liu, C.; Zhang, L.; Li, Y.; Zhou, X.; She, S.; Wang, X.; Tian, Y.; Jen, A. K. Y.; Xu, B. Highly Stable and Efficient Perovskite Solar Cells with 22.0% Efficiency Based on Inorganic–Organic Dopant-Free Double Hole Transporting Layers. *Adv. Funct. Mater.* **2020**, *30* (28), 1908462. <https://doi.org/10.1002/adfm.201908462>.
 - (35) Khattak, Y. H.; Baig, F.; Toura, H.; Beg, S.; Soucase, B. M. CZTSe Kesterite as an Alternative Hole Transport Layer for MASnI₃ Perovskite Solar Cells. *J. Electron. Mater.* **2019**, *48* (9), 5723–5733. <https://doi.org/10.1007/s11664-019-07374-5>.
 - (36) Chen, J.; Park, N.-G. Inorganic Hole Transporting Materials for Stable and High Efficiency Perovskite Solar Cells. *J. Phys. Chem. C* **2018**, *122* (25), 14039–14063. <https://doi.org/10.1021/acs.jpcc.8b01177>.
 - (37) Shin, D.; Saporov, B.; Zhu, T.; Huhn, W. P.; Blum, V.; Mitzi, D. B. BaCu₂Sn(S,Se)₄: Earth-Abundant Chalcogenides for Thin-Film Photovoltaics. *Chem. Mater.* **2016**, *28* (13), 4771–4780. <https://doi.org/10.1021/acs.chemmater.6b01832>.
 - (38) Chakraborty, R.; Sim, K. M.; Shrivastava, M.; Adarsh, K. V.; Chung, D. S.; Nag, A. Colloidal Synthesis, Optical Properties, and Hole Transport Layer Applications of Cu₂BaSnS₄ (CBTS) Nanocrystals. *ACS Appl.*

- Energy Mater.* **2019**, *2* (5), 3049–3055. <https://doi.org/10.1021/acsaem.9b00473>.
- (39) Clark, S. J.; Segall, M. D.; Pickard, C. J.; Hasnip, P. J.; Probert, M. I. J.; Refson, K.; Payne, M. C. First Principles Methods Using CASTEP. *Zeitschrift für Krist. - Cryst. Mater.* **2005**, *220* (5–6), 567–570. <https://doi.org/10.1524/zkri.220.5.567.65075>.
- (40) Perdew, J. P.; Ruzsinszky, A.; Csonka, G. I.; Vydrov, O. A.; Scuseria, G. E.; Constantin, L. A.; Zhou, X.; Burke, K. Restoring the Density-Gradient Expansion for Exchange in Solids and Surfaces. *Phys. Rev. Lett.* **2008**, *100* (13), 136406. <https://doi.org/10.1103/PhysRevLett.100.136406>.
- (41) Vanderbilt, D. Soft Self-Consistent Pseudopotentials in a Generalized Eigenvalue Formalism. *Phys. Rev. B* **1990**, *41* (11), 7892–7895. <https://doi.org/10.1103/PhysRevB.41.7892>.
- (42) Head, J. D.; Zerner, M. C. A Broyden—Fletcher—Goldfarb—Shanno Optimization Procedure for Molecular Geometries. *Chem. Phys. Lett.* **1985**, *122* (3), 264–270. [https://doi.org/10.1016/0009-2614\(85\)80574-1](https://doi.org/10.1016/0009-2614(85)80574-1).
- (43) Monkhorst, H. J.; Pack, J. D. Special Points for Brillouin-Zone Integrations. *Phys. Rev. B* **1976**, *13* (12), 5188–5192. <https://doi.org/10.1103/PhysRevB.13.5188>.
- (44) Decock, K.; Niemegeers, A.; Verschraegen, J. SCAPS Manual Most Recent. **2021**.
- (45) Burgelman, M.; Nollet, P.; Degraeve, S. Modelling Polycrystalline Semiconductor Solar Cells. *Thin Solid Films* **2000**, *361–362*, 527–532. [https://doi.org/10.1016/S0040-6090\(99\)00825-1](https://doi.org/10.1016/S0040-6090(99)00825-1).
- (46) Islam, M. T.; Jani, M. R.; Shorowordi, K. M.; Hoque, Z.; Gokcek, A. M.; Vattipally, V.; Nishat, S. S.; Ahmed, S. Numerical Simulation Studies of Cs₃Bi₂I₉ Perovskite Solar Device with Optimal Selection of Electron and Hole Transport Layers. *Optik (Stuttg.)*. **2021**, *231* (January), 166417. <https://doi.org/10.1016/j.ijleo.2021.166417>.
- (47) Islam, M. T.; Jani, M. R.; Al Amin, S. M.; Sami, M. S. U.; Shorowordi, K. M.; Hossain, M. I.; Devgun, M.; Chowdhury, S.; Banerje, S.; Ahmed, S. Numerical Simulation Studies of a Fully Inorganic Cs₂AgBiBr₆ Perovskite Solar Device. *Opt. Mater. (Amst.)*. **2020**, *105*, 109957. <https://doi.org/10.1016/j.optmat.2020.109957>.
- (48) Alam, I.; Mollick, R.; Ashraf, M. A. Numerical Simulation of Cs₂AgBiBr₆-Based Perovskite Solar Cell with ZnO Nanorod and P3HT as the Charge Transport Layers. *Phys. B Condens. Matter* **2021**, *618*, 413187. <https://doi.org/10.1016/j.physb.2021.413187>.
- (49) Farhana Anwar, Sajia Afrin, Sakin Sarwar Satter, Rafee Mahbub, S. M. U. Simulation and Performance Study of Nanowire CdS/CdTe Solar Cell. *Int. J. Renew. Energy Res.* **2017**, No. v7i2. <https://doi.org/10.20508/ijrer.v7i2.5688.g7068>.
- (50) Moon, M. M. A.; Ali, M. H.; Rahman, M. F.; Kuddus, A.; Hossain, J.; Ismail, A. B. M. Investigation of Thin-Film p -BaSi₂/n -CdS Heterostructure towards Semiconducting Silicide Based High Efficiency Solar Cell. *Phys. Scr.* **2020**, *95* (3), 035506. <https://doi.org/10.1088/1402-4896/ab49e8>.
- (51) Noorasid, N. S.; Arith, F.; Firhat, A. Y. SCAPS Numerical Analysis of Solid-State Dye- Sensitized Solar Cell Utilizing Copper (I) Iodide as Hole Transport Layer. *Eng. J.* **22AD**, *26* (2), 1–10. <https://doi.org/10.4186/ej.2022.26.2.1>.
- (52) Chabri, I.; Oubelkacem, A.; Benhouria, Y. Numerical Development of Lead-Free Cs₂TiI₆-Based Perovskite Solar Cell via SCAPS-1D. *E3S Web Conf.* **2022**, *336*, 00050. <https://doi.org/10.1051/e3sconf/202233600050>.
- (53) Deepthi Jayan, K.; Sebastian, V. Modelling and Comparative Performance Analysis of Tin Based Mixed Halide Perovskite Solar Cells with IGZO and CuO as Charge Transport Layers. *Int. J. Energy Res.* **2021**, *45* (11), 16618–16632. <https://doi.org/10.1002/er.6909>.
- (54) Hima, A. Enhancing of CH₃NH₃SnI₃ Based Solar Cell Efficiency by ETL Engineering. *Int. J. Energ.* **2020**, *5* (1), 27. <https://doi.org/10.47238/ijeca.v5i1.119>.
- (55) Sobayel, K.; Akhtaruzzaman, M.; Rahman, K. S.; Ferdaous, M. T.; Al-Mutairi, Z. A.; Alharbi, H. F.; Alharthi, N. H.; Karim, M. R.; Hasmady, S.; Amin, N. A Comprehensive Defect Study of Tungsten Disulfide (WS₂) as Electron Transport Layer in Perovskite Solar Cells by Numerical Simulation. *Results Phys.* **2019**, *12*, 1097–1103. <https://doi.org/10.1016/j.rinp.2018.12.049>.
- (56) Ahmmmed, S.; Aktar, A.; Hossain, J.; Ismail, A. B. M. Enhancing the Open Circuit Voltage of the SnS Based Heterojunction Solar Cell Using NiO HTL. *Sol. Energy* **2020**, *207*, 693–702. <https://doi.org/10.1016/j.solener.2020.07.003>.
- (57) Wang, Y.; Xia, Z.; Liu, Y.; Zhou, H. Simulation of Perovskite Solar Cells with Inorganic Hole Transporting Materials. *2015 IEEE 42nd Photovolt. Spec. Conf. PVSC 2015* **2015**, 3–6.

- <https://doi.org/10.1109/PVSC.2015.7355717>.
- (58) Touafek, N.; Mahamdi, R.; Dridi, C. Boosting the Performance of Planar Inverted Perovskite Solar Cells Employing Graphene Oxide as HTL. *2021*, *16* (2), 705–712.
 - (59) Alipour, H.; Ghadimi, A. Optimization of Lead-Free Perovskite Solar Cells in Normal-Structure with and Water-Free PEDOT: PSS Composite for Hole Transport Layer by SCAPS-1D Simulation. *Opt. Mater. (Amst)*. **2021**, *120*, 111432. <https://doi.org/10.1016/j.optmat.2021.111432>.
 - (60) Huang, L.; Sun, X.; Li, C.; Xu, R.; Xu, J.; Du, Y.; Wu, Y.; Ni, J.; Cai, H.; Li, J.; Hu, Z.; Zhang, J. Electron Transport Layer-Free Planar Perovskite Solar Cells: Further Performance Enhancement Perspective from Device Simulation. *Sol. Energy Mater. Sol. Cells* **2016**, *157*, 1038–1047. <https://doi.org/10.1016/j.solmat.2016.08.025>.
 - (61) Moulaoui, L.; Bajjou, O.; Najim, A.; Archi, M.; Rahmani, K. Numerical Simulation of the NiO as Hole Transport Layer in $\text{CH}_3\text{NH}_3\text{PbBr}_3$ Perovskite Based-Solar Cell Using SCAPS-1D. In *2022 2nd International Conference on Innovative Research in Applied Science, Engineering and Technology (IRASET)*; IEEE, 2022; pp 1–7. <https://doi.org/10.1109/IRASET52964.2022.9737984>.
 - (62) Khatun, M. M.; Sunny, A.; Ahmed, S. R. Al. Numerical Investigation on Performance Improvement of WS_2 Thin-Film Solar Cell with Copper Iodide as Hole Transport Layer. *Sol. Energy* **2021**, *224* (July), 956–965. <https://doi.org/10.1016/j.solener.2021.06.062>.
 - (63) Sawicka-Chudy, P.; Starowicz, Z.; Wisz, G.; Yavorskyi, R.; Zapukhlyak, Z.; Bester, M.; Głowa, Ł.; Sibiński, M.; Cholewa, M. Simulation of TiO_2/CuO Solar Cells with SCAPS-1D Software. *Mater. Res. Express* **2019**, *6* (8), 085918. <https://doi.org/10.1088/2053-1591/ab22aa>.
 - (64) Kuddus, A.; Rahman, M. F.; Ahmmed, S.; Hossain, J.; Ismail, A. B. M. Role of Facile Synthesized V_2O_5 as Hole Transport Layer for CdS/CdTe Heterojunction Solar Cell: Validation of Simulation Using Experimental Data. *Superlattices Microstruct.* **2019**, *132*, 106168. <https://doi.org/10.1016/j.spmi.2019.106168>.
 - (65) Guechi, N.; Bouhemadou, A.; Bin-Omran, S.; Bourzami, A.; Louail, L. Elastic, Optoelectronic and Thermoelectric Properties of the Lead-Free Halide Semiconductors $\text{Cs}_2\text{AgBiX}_6$ ($X = \text{Cl}, \text{Br}$): Ab Initio Investigation. *J. Electron. Mater.* **2018**, *47* (2), 1533–1545. <https://doi.org/10.1007/s11664-017-5962-2>.
 - (66) Irfan, M.; Azam, S.; Hussain, S.; Khan, S. A.; Sohail, M.; Ahmad, M.; Goumri-Said, S. Enhanced Thermoelectric Properties of ASbO_3 Due to Decreased Band Gap through Modified Becke Johnson Potential Scheme. *J. Phys. Chem. Solids* **2018**, *119*, 85–93. <https://doi.org/10.1016/j.jpics.2018.03.010>.
 - (67) Murtaza, G.; Ahmad, I. First Principle Study of the Structural and Optoelectronic Properties of Cubic Perovskites CsPbM_3 ($M = \text{Cl}, \text{Br}, \text{I}$). *Phys. B Condens. Matter* **2011**, *406* (17), 3222–3229. <https://doi.org/10.1016/j.physb.2011.05.028>.
 - (68) Lang, L.; Yang, J.-H.; Liu, H.-R.; Xiang, H. J.; Gong, X. G. First-Principles Study on the Electronic and Optical Properties of Cubic ABX_3 Halide Perovskites. *Phys. Lett. A* **2014**, *378* (3), 290–293. <https://doi.org/10.1016/j.physleta.2013.11.018>.
 - (69) Nishio, T.; Ahmad, J.; Uwe, H. Spectroscopic Observation of Bipolaronic Point Defects in $\text{Ba}_{1-x}\text{K}_x\text{BiO}_3$. *Phys. Rev. Lett.* **2005**, *95* (17), 176403. <https://doi.org/10.1103/PhysRevLett.95.176403>.
 - (70) Rubel, M. H. K.; Hossain, M. A.; Hossain, M. K.; Hossain, K. M.; Khatun, A. A.; Rahaman, M. M.; Ferdous Rahman, M.; Hossain, M. M.; Hossain, J. First-Principles Calculations to Investigate Structural, Elastic, Electronic, Thermodynamic, and Thermoelectric Properties of $\text{CaPd}_3\text{B}_4\text{O}_{12}$ ($B = \text{Ti}, \text{V}$) Perovskites. *Results Phys.* **2022**, *42*, 105977. <https://doi.org/10.1016/j.rinp.2022.105977>.
 - (71) Rubel, M. H. K.; Mitro, S. K.; Hossain, M. K.; Hossain, K. M.; Rahaman, M. M.; Hossain, J.; Mondal, B. K.; Akter, A.; Rahman, M. F.; Ahmed, I.; Islam, A. K. M. A. First-Principles Calculations to Investigate Physical Properties of Single-Cubic $(\text{Ba}_{0.82}\text{K}_{0.18})(\text{Bi}_{0.53}\text{Pb}_{0.47})\text{O}_3$ Novel Perovskite Superconductor. *Mater. Today Commun.* **2022**, *33*, 104302. <https://doi.org/10.1016/j.mtcomm.2022.104302>.
 - (72) Lin, Z.; Lei, J.; Wang, P.; Zhang, X.; Xu, L.; Chen, M.; Kang, Y.; Wei, G. Density Functional Study of Structural, Electronic and Optical Properties of Bromine-Doped CsPbI_3 with the Tetragonal Symmetry. *J. Alloys Compd.* **2022**, *892*, 162165. <https://doi.org/10.1016/j.jallcom.2021.162165>.
 - (73) Ali, M. A.; Anwar Hossain, M.; Rayhan, M. A.; Hossain, M. M.; Uddin, M. M.; Roknuzzaman, M.; Ostrikov, K.; Islam, A. K. M. A.; Naqib, S. H. First-Principles Study of Elastic, Electronic, Optical and Thermoelectric Properties of Newly Synthesized $\text{K}_2\text{Cu}_2\text{GeS}_4$ Chalcogenide. *J. Alloys Compd.* **2019**, *781*, 37–46. <https://doi.org/10.1016/j.jallcom.2018.12.035>.
 - (74) Li, S.; Ahuja, R.; Barsoum, M. W.; Jena, P.; Johansson, B. Optical Properties of Ti_3SiC_2 and Ti_4AlN_3 .

- Appl. Phys. Lett.* **2008**, *92* (22), 221907. <https://doi.org/10.1063/1.2938862>.
- (75) Okoye, C. M. I. Optical Properties of the Antiperovskite Superconductor MgCNi₃. *J. Phys. Condens. Matter* **2003**, *15* (6), 833–841. <https://doi.org/10.1088/0953-8984/15/6/310>.
- (76) Afsari, M.; Boochani, A.; Hantezadeh, M. Electronic, Optical and Elastic Properties of Cubic Perovskite CsPbI₃: Using First Principles Study. *Optik (Stuttg.)* **2016**, *127* (23), 11433–11443. <https://doi.org/10.1016/j.ijleo.2016.09.013>.
- (77) Fox, M. *Optical Properties of Solids*; Academic Press: New York, USA.
- (78) Mandadapu, U.; Vedanayakam, S. V.; Thyagarajan, K. Simulation and Analysis of Lead Based Perovskite Solar Cell Using SCAPS-1D. *Indian J. Sci. Technol.* **2017**, *10* (11), 1–8. <https://doi.org/10.17485/ijst/2017/v10i11/110721>.
- (79) Ahmad, O.; Rashid, A.; Ahmed, M. W.; Nasir, M. F.; Qasim, I. Performance Evaluation of Au/p-CdTe/Cs₂TiI₆/n-TiO₂/ITO Solar Cell Using SCAPS-1D. *Opt. Mater. (Amst.)* **2021**, *117*, 111105. <https://doi.org/10.1016/j.optmat.2021.111105>.
- (80) Bag, A.; Radhakrishnan, R.; Nekovei, R.; Jeyakumar, R. Effect of Absorber Layer, Hole Transport Layer Thicknesses, and Its Doping Density on the Performance of Perovskite Solar Cells by Device Simulation. *Sol. Energy* **2020**, *196*, 177–182. <https://doi.org/10.1016/j.solener.2019.12.014>.
- (81) Bosio, A.; Pasini, S.; Romeo, N. The History of Photovoltaics with Emphasis on CdTe Solar Cells and Modules. *Coatings* **2020**, *10* (4), 344. <https://doi.org/10.3390/coatings10040344>.
- (82) Rahman, M. F.; Habib, M. J. A.; Ali, M. H.; Rubel, M. H. K.; Islam, M. R.; Ismail, A. B. M.; Hossain, M. K. Design and Numerical Investigation of Cadmium Telluride (CdTe) and Iron Silicide (FeSi₂) Based Double Absorber Solar Cells to Enhance Power Conversion Efficiency. *AIP Adv.* **2022**, *12*, 105317. <https://doi.org/10.1063/5.0108459>.
- (83) Raga, S. R.; Barea, E. M.; Fabregat-Santiago, F. Analysis of the Origin of Open Circuit Voltage in Dye Solar Cells. *J. Phys. Chem. Lett.* **2012**, *3* (12), 1629–1634. <https://doi.org/10.1021/jz3005464>.
- (84) Behrouznejad, F.; Shahbazi, S.; Taghavinia, N.; Wu, H.-P.; Wei-Guang Diao, E. A Study on Utilizing Different Metals as the Back Contact of CH₃NH₃PbI₃ Perovskite Solar Cells. *J. Mater. Chem. A* **2016**, *4* (35), 13488–13498. <https://doi.org/10.1039/C6TA05938D>.
- (85) Decock, K.; Khelifi, S.; Burgelman, M. Modelling Multivalent Defects in Thin Film Solar Cells. *Thin Solid Films* **2011**, *519* (21), 7481–7484. <https://doi.org/10.1016/j.tsf.2010.12.039>.
- (86) Samiul Islam, M.; Sobayel, K.; Al-Kahtani, A.; Islam, M. A.; Muhammad, G.; Amin, N.; Shahiduzzaman, M.; Akhtaruzzaman, M. Defect Study and Modelling of SnX₃-Based Perovskite Solar Cells with SCAPS-1D. *Nanomaterials* **2021**, *11* (5), 1218. <https://doi.org/10.3390/nano11051218>.
- (87) Mamta; Maurya, K. K.; Singh, V. N. Sb₂Se₃/CZTS Dual Absorber Layer Based Solar Cell with 36.32 % Efficiency: A Numerical Simulation. *J. Sci. Adv. Mater. Devices* **2022**, *7* (2), 100445. <https://doi.org/10.1016/j.jsamd.2022.100445>.
- (88) Shivesh, K.; Alam, I.; Kushwaha, A. K.; Kumar, M.; Singh, S. V. Investigating the Theoretical Performance of Cs₂TiBr₆-Based Perovskite Solar Cell with La-Doped BaSnO₃ and CuSbS₂ as the Charge Transport Layers. *Int. J. Energy Res.* **2022**, *46* (5), 6045–6064. <https://doi.org/10.1002/er.7546>.
- (89) Wang, K.; Jin, Z.; Liang, L.; Bian, H.; Wang, H.; Feng, J.; Wang, Q.; Liu, S. (Frank). Chlorine Doping for Black γ -CsPbI₃ Solar Cells with Stabilized Efficiency beyond 16%. *Nano Energy* **2019**, *58*, 175–182. <https://doi.org/10.1016/j.nanoen.2019.01.034>.
- (90) Wang, Y.; Liu, X.; Zhang, T.; Wang, X.; Kan, M.; Shi, J.; Zhao, Y. The Role of Dimethylammonium Iodide in CsPbI₃ Perovskite Fabrication: Additive or Dopant? *Angew. Chemie Int. Ed.* **2019**, *58* (46), 16691–16696. <https://doi.org/10.1002/anie.201910800>.
- (91) Frolova, L. A.; Anokhin, D. V.; Piryazev, A. A.; Luchkin, S. Y.; Dremova, N. N.; Stevenson, K. J.; Troshin, P. A. Highly Efficient All-Inorganic Planar Heterojunction Perovskite Solar Cells Produced by Thermal Coevaporation of CsI and PbI₂. *J. Phys. Chem. Lett.* **2017**, *8* (1), 67–72. <https://doi.org/10.1021/acs.jpcclett.6b02594>.
- (92) Zhao, B.; Jin, S.-F.; Huang, S.; Liu, N.; Ma, J.-Y.; Xue, D.-J.; Han, Q.; Ding, J.; Ge, Q.-Q.; Feng, Y.; Hu, J.-S. Thermodynamically Stable Orthorhombic γ -CsPbI₃ Thin Films for High-Performance Photovoltaics. *J. Am. Chem. Soc.* **2018**, *140* (37), 11716–11725. <https://doi.org/10.1021/jacs.8b06050>.
- (93) Xiang, S.; Fu, Z.; Li, W.; Wei, Y.; Liu, J.; Liu, H.; Zhu, L.; Zhang, R.; Chen, H. Highly Air-Stable Carbon-Based α -CsPbI₃ Perovskite Solar Cells with a Broadened Optical Spectrum. *ACS Energy Lett.* **2018**, *3* (8), 1824–1831. <https://doi.org/10.1021/acsenergylett.8b00820>.

- (94) Becker, P.; Márquez, J. A.; Just, J.; Al-Ashouri, A.; Hages, C.; Hempel, H.; Jošt, M.; Albrecht, S.; Frahm, R.; Unold, T. Low Temperature Synthesis of Stable Γ -CsPbI₃ Perovskite Layers for Solar Cells Obtained by High Throughput Experimentation. *Adv. Energy Mater.* **2019**, *9* (22), 1900555. <https://doi.org/10.1002/aenm.201900555>.
- (95) Ke, W.; Spanopoulos, I.; Stoumpos, C. C.; Kanatzidis, M. G. Myths and Reality of HPbI₃ in Halide Perovskite Solar Cells. *Nat. Commun.* **2018**, *9* (1), 4785. <https://doi.org/10.1038/s41467-018-07204-y>.
- (96) Xi, J.; Piao, C.; Byeon, J.; Yoon, J.; Wu, Z.; Choi, M. Rational Core–Shell Design of Open Air Low Temperature In Situ Processable CsPbI₃ Quasi-Nanocrystals for Stabilized P-i-n Solar Cells. *Adv. Energy Mater.* **2019**, *9* (31), 1901787. <https://doi.org/10.1002/aenm.201901787>.
- (97) Swarnkar, A.; Marshall, A. R.; Sanehira, E. M.; Chernomordik, B. D.; Moore, D. T.; Christians, J. A.; Chakrabarti, T.; Luther, J. M. Quantum Dot–Induced Phase Stabilization of α -CsPbI₃ Perovskite for High-Efficiency Photovoltaics. *Science* (80-.). **2016**, *354* (6308), 92–95. <https://doi.org/10.1126/science.aag2700>.
- (98) Li, B.; Zhang, Y.; Fu, L.; Yu, T.; Zhou, S.; Zhang, L.; Yin, L. Surface Passivation Engineering Strategy to Fully-Inorganic Cubic CsPbI₃ Perovskites for High-Performance Solar Cells. *Nat. Commun.* **2018**, *9* (1), 1076. <https://doi.org/10.1038/s41467-018-03169-0>.
- (99) Luo, P.; Xia, W.; Zhou, S.; Sun, L.; Cheng, J.; Xu, C.; Lu, Y. Solvent Engineering for Ambient-Air-Processed, Phase-Stable CsPbI₃ in Perovskite Solar Cells. *J. Phys. Chem. Lett.* **2016**, *7* (18), 3603–3608. <https://doi.org/10.1021/acs.jpcclett.6b01576>.
- (100) Wang, K.; Li, Z.; Zhou, F.; Wang, H.; Bian, H.; Zhang, H.; Wang, Q.; Jin, Z.; Ding, L.; Liu, S. (Frank). Ruddlesden–Popper 2D Component to Stabilize Γ -CsPbI₃ Perovskite Phase for Stable and Efficient Photovoltaics. *Adv. Energy Mater.* **2019**, *9* (42), 1902529. <https://doi.org/10.1002/aenm.201902529>.
- (101) Bian, H.; Bai, D.; Jin, Z.; Wang, K.; Liang, L.; Wang, H.; Zhang, J.; Wang, Q.; Liu, S. (Frank). Graded Bandgap CsPbI₂⁺Br¹⁻ Perovskite Solar Cells with a Stabilized Efficiency of 14.4%. *Joule* **2018**, *2* (8), 1500–1510. <https://doi.org/10.1016/j.joule.2018.04.012>.
- (102) Liu, F.; Ding, C.; Zhang, Y.; Kamisaka, T.; Zhao, Q.; Luther, J. M.; Toyoda, T.; Hayase, S.; Minemoto, T.; Yoshino, K.; Zhang, B.; Dai, S.; Jiang, J.; Tao, S.; Shen, Q. GeI₂ Additive for High Optoelectronic Quality CsPbI₃ Quantum Dots and Their Application in Photovoltaic Devices. *Chem. Mater.* **2019**, *31* (3), 798–807. <https://doi.org/10.1021/acs.chemmater.8b03871>.

SUPPORTING INFORMATION

Table of content

Figure S1.	Energy level alignment of studied ITO, 9 ETLs, CsPbI ₃ , and 12 HTLs	33
Figure S2.	Best optimized structures of CsPbI ₃ -based PSC with CBTS as the HTL and PCBM, TiO ₂ , ZnO, C ₆₀ , IGZO, and WS ₂ as ETLs	34
Figure S3.	Effect of the variation in temperature from 275 K to 475 K on V_{OC} , J_{SC} , FF , and PCE	35

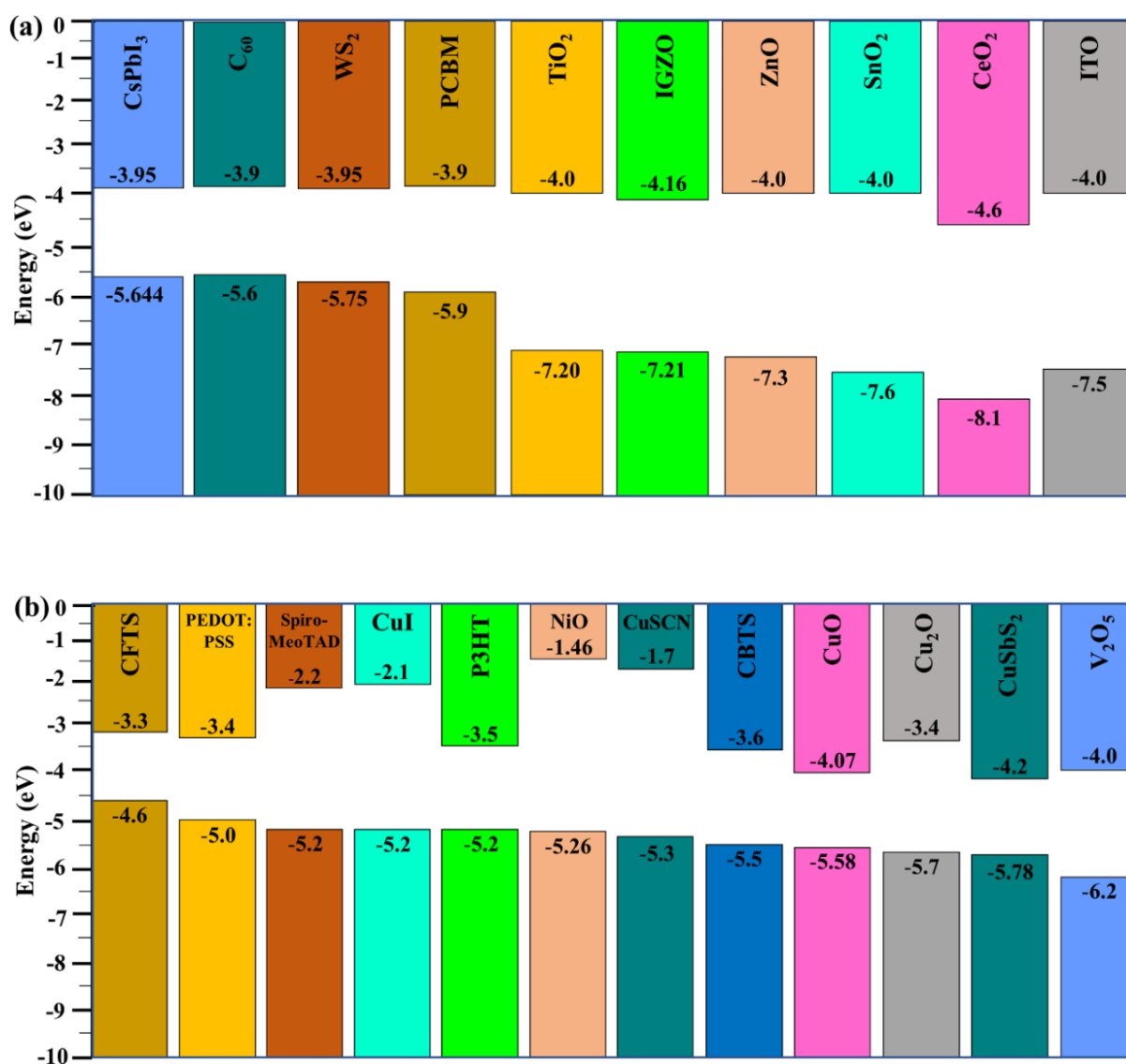


Figure S1: Energy level alignment of studied (a) ITO, ETLs, and absorber CsPbI₃, and (b) HTLs.

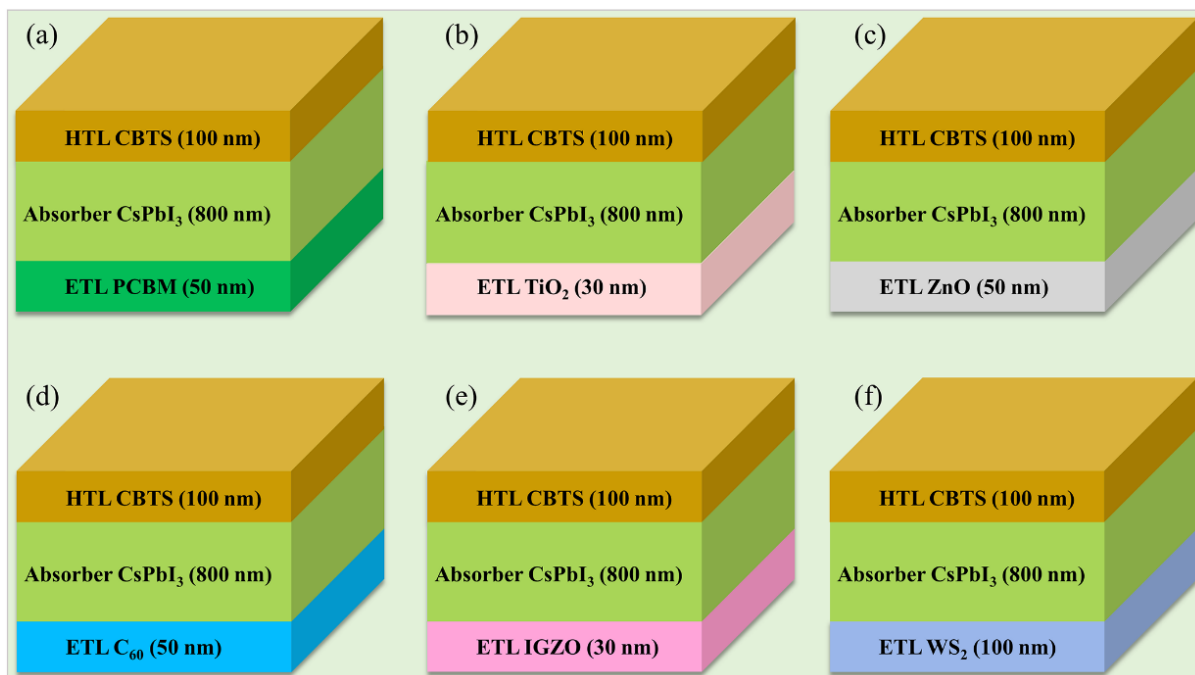


Figure S2. Best optimized structures of CsPbI₃-based PSC with CBTS as the HTL and (a) PCBM, (b) TiO₂, (c) ZnO, (d) C₆₀, (e) IGZO, and (f) WS₂ as the ETLs.

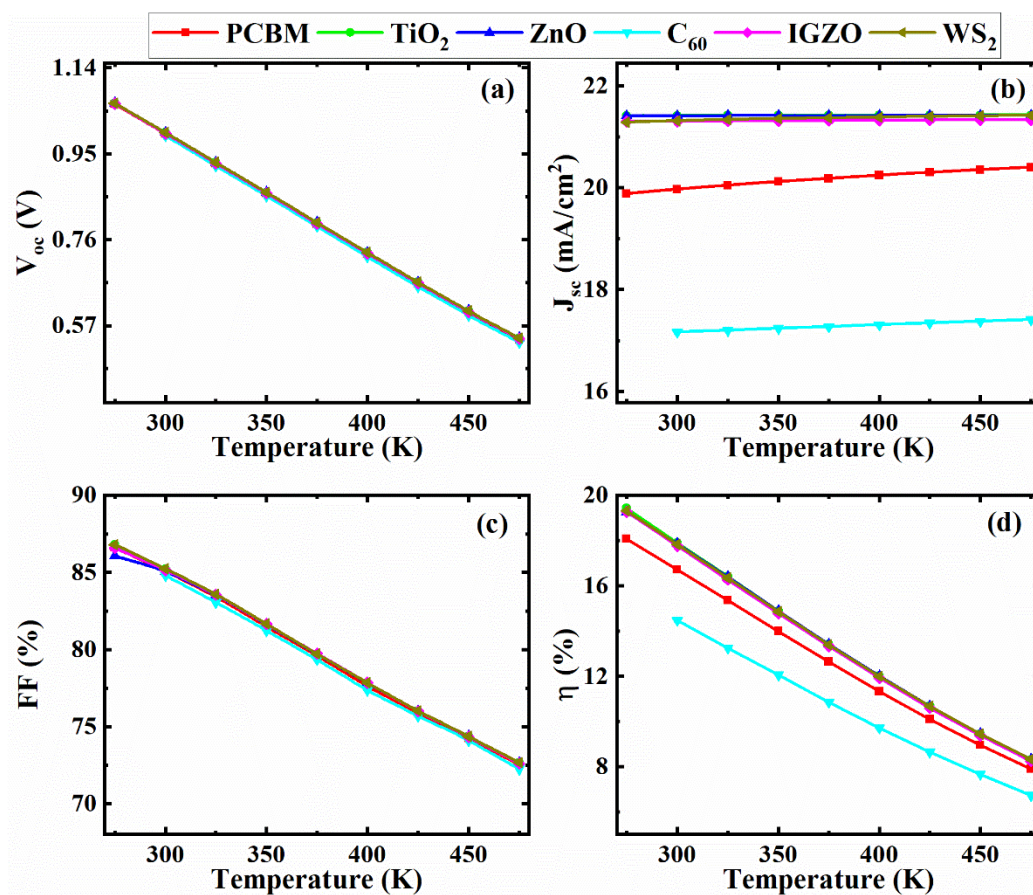


Figure S3. Effect of the variation in temperature from 275 K to 475 K on (a) V_{oc} , (b) J_{sc} , (c) FF, and (d) PCE.